**Article**

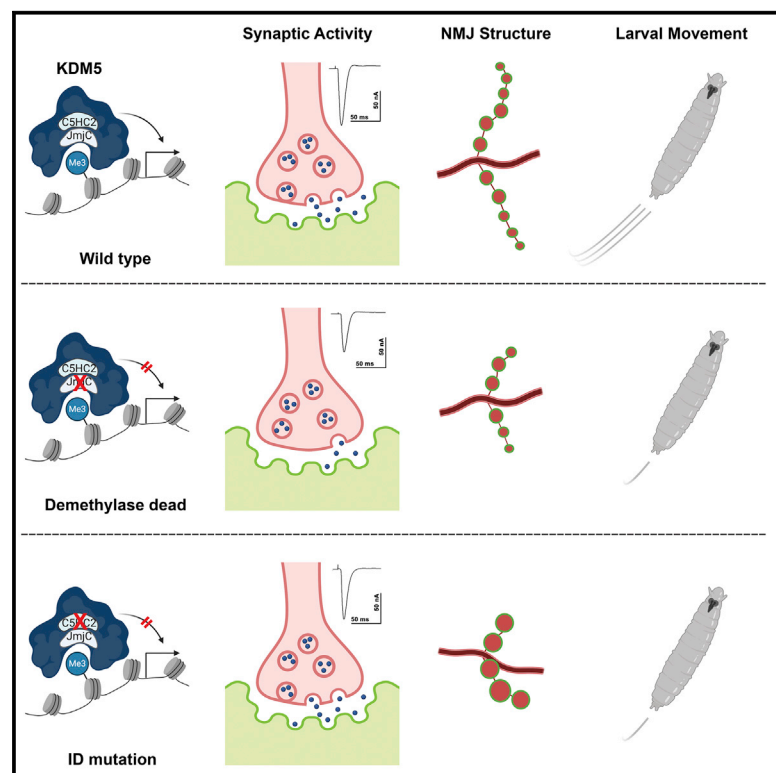# The histone demethylase KDM5 is required for synaptic structure and function at the *Drosophila* neuromuscular junction

## Graphical Abstract



## Highlights

- *Drosophila* KDM5 regulates transcriptional programs vital to synaptic development

- KDM5 uses demethylase-dependent and independent means to regulate NMJ development

- The demethylase activity of KDM5 promotes bouton number and neurotransmission

- The C5HC2 motif of KDM5 is needed for neuroanatomical development

## Authors

Helen M. Belalcazar, Emily L. Hendricks, Sumaira Zamurrad, Faith L.W. Liebl, Julie Secombe

## Correspondence

julie.secombe@einsteinmed.org

## In Brief

Mutations in the KDM5 family of histone demethylases are observed in individuals with intellectual disability (ID). Belalcazar et al. show that KDM5-regulated transcription is necessary in *Drosophila* for proper neuroanatomical development and neurotransmission at the glutamatergic larval neuromuscular junction.

CellPress

## Article

# The histone demethylase KDM5 is required for synaptic structure and function at the *Drosophila* neuromuscular junction

Helen M. Belalcazar,[1] Emily L. Hendricks,[2] Sumaira Zamurrad,[1,4] Faith L.W. Liebl,[2] and Julie Secombe[1,3,5,*]

[1]Department of Genetics, Albert Einstein College of Medicine, 1300 Morris Park Avenue, Bronx, NY 10461, USA
[2]Department of Biological Sciences, Southern Illinois University Edwardsville, 44 Circle Drive, Edwardsville, IL 62026, USA
[3]Dominick P. Purpura Department of Neuroscience, Albert Einstein College of Medicine, 1410 Pelham Parkway South, Bronx, NY 10461, USA
[4]Present address: Columbia University, 3227 Broadway, Quad 9A, MC9891, New York, NY 10027, USA
[5]Lead contact
*Correspondence: julie.secombe@einsteinmed.org
https://doi.org/10.1016/j.celrep.2021.108753

## SUMMARY

Mutations in the genes encoding the lysine demethylase 5 (KDM5) family of histone demethylases are observed in individuals with intellectual disability (ID). Despite clear evidence linking KDM5 function to neurodevelopmental pathways, how this family of proteins impacts transcriptional programs to mediate synaptic structure and activity remains unclear. Using the *Drosophila* larval neuromuscular junction (NMJ), we show that KDM5 is required presynaptically for neuroanatomical development and synaptic function. The Jumonji C (JmjC) domain-encoded histone demethylase activity of KDM5, which is expected to be diminished by many ID-associated alleles, is required for appropriate synaptic morphology and neurotransmission. The activity of the C5HC2 zinc finger is also required, as an ID-associated mutation in this motif reduces NMJ bouton number, increases bouton size, and alters microtubule dynamics. KDM5 therefore uses demethylase-dependent and independent mechanisms to regulate NMJ structure and activity, highlighting the complex nature by which this chromatin modifier carries out its neuronal gene-regulatory programs.

## INTRODUCTION

Dysregulation of gene expression in the central nervous system (CNS) has profound effects on cognitive and other neurological functions (Ronan et al., 2013). The recent expansion of genomic analyses in patients with neurodevelopmental disorders (NDDs) has dramatically increased our understanding of the transcriptional regulators that might contribute to cognitive impairment. These studies have revealed 122 distinct variants in the lysine demethylase 5 (KDM5) family genes *KDM5A*, *KDM5B*, and *KDM5C* that encode chromatin modifier proteins in individuals with NDDs, particularly intellectual disability (ID) (Kim et al., 2017; Vallianatos and Iwase, 2015).

KDM5 proteins are gene expression regulators that enzymatically remove di- and/or trimethylated lysine 4 of histone H3 (H3K4me2/3) through the activity of a conserved Jumonji C (JmjC) domain (Hyun et al., 2017). The H3K4me2/3 chromatin marks are predominantly found at the promoter region of transcriptionally active genes and changes to these histone modifications can impact transcriptional consistency (Barski et al., 2007; Benayoun et al., 2014). Prevailing models of *KDM5*-induced ID suggest that it is the loss of histone demethylase activity that drives the neuropathologies observed in patients. In support of this, *in vitro* studies using recombinant KDM5C harboring ID-associated variants showed reduced activity toward a histone peptide substrate (Iwase et al., 2007; Rujirabanjerd et al., 2010; Tahiliani et al., 2007). Consistent with this observation, a *Drosophila* mutant specifically lacking KDM5 demethylase activity shows learning and memory deficits (Zamurrad et al., 2018). Additionally, the cognitive deficits observed in *Kdm5c* knockout mice can be partially ameliorated by genetically lowering levels of the H3K4 methyltransferase KMT2A (*Kmt2a* heterozygotes) (Vallianatos et al., 2020). Contrasting these findings, some ID-associated mutations in *KDM5C* do not cause deficits to *in vitro* demethylase activity (Tahiliani et al., 2007; Vallianatos et al., 2018). Both non-enzymatic and enzymatic mechanisms of gene regulation by KDM5 family proteins may therefore be important for neuronal function.

There is still much to be learned regarding the cellular consequences of mutations in *KDM5* family genes. Structural changes in neuronal morphology and circuitry are often observed in postmortem brain samples from individuals with neurodevelopmental and neuropsychiatric disorders (Forrest et al., 2018). These analyses have yet to be performed in patients with mutations in *KDM5* family genes. However, model organisms have provided insights about the consequences of KDM5 loss of function on neuronal morphology. For example, knockdown of *Kdm5c* in cultured rat cerebellar granular neurons results in changes in dendritic arborization (Iwase et al., 2007) and *Kdm5c* knockout mice show decreased cortical neuron spine

density (Iwase et al., 2016; Scandaglia et al., 2017). Although dendritic spine morphology can be altered by neuronal activity (Nägerl et al., 2004; Verpelli et al., 2010), the extent to which synaptic function is disrupted by mutations in *KDM5* genes remains uncharacterized.

To further our understanding of the link between KDM5-regulated transcription and neuronal development, we examined its function at the *Drosophila* neuromuscular junction (NMJ). This glutamatergic synapse is a well-established model for addressing questions of neural development, morphology, and synaptic function, as it requires proteins homologous to those found in mammalian CNS excitatory synapses (Koh et al., 2000; Li et al., 2007; Rasse et al., 2005; Roos et al., 2000). Mutations in the orthologs of human ID-associated genes that encode synaptic proteins found at glutamatergic terminals such as ionotropic and metabotropic glutamate receptors, the scaffold protein PSD95/Dlg, the phosphoprotein synapsin, and the cell-adhesion proteins neurexin and neuroligin (Moretto et al., 2018; Volk et al., 2015) cause structural and functional alterations at the *Drosophila* NMJ (Budnik et al., 1996; DiAntonio, 2006; Vasin et al., 2014; Xing et al., 2018). *Drosophila* encodes a single KDM5 ortholog (also known as Lid) that shares homology with all four mammalian KDM5 proteins. Thus, *in vivo* analyses of KDM5 are expected to reveal activities relevant to *KDM5A*-, *KDM5B*-, and *KDM5C*-induced ID. In this study, we show that KDM5 is required presynaptically within motor neurons for proper NMJ morphology and function. The histone demethylase activity of KDM5 is a key contributor to its synaptic functions, as animals lacking this activity show a reduced number of synaptic boutons and a decrease in evoked glutamate release. Additionally, we find that KDM5's neuroregulatory functions require the C5HC2 zinc-finger motif, which has no currently known function. This is based on our analyses of a variant within the C5HC2 motif of KDM5, equivalent to an ID-associated variant in *KDM5C*, that reduces the number of synaptic boutons and increases their size. Interestingly, this ID-associated allele does not appear to dramatically alter histone demethylase activity, suggesting that KDM5 uses enzymatic and non-enzymatic mechanisms of gene regulation to properly form and maintain NMJs. Consistent with these data, RNA-sequencing (RNA-seq) analyses of the ventral nerve cord (VNC), where the nuclei of motor neurons reside, revealed that mutations in the JmjC domain or C5HC2 motif cause distinct transcriptional changes. Combined, these data advance our understanding of the neuronal activities of KDM5 and highlight the importance of discrete domains that mediate its gene-regulatory programs in neurons.

## RESULTS

### KDM5 is required presynaptically for proper NMJ structure

During *Drosophila* embryonic development, motor neuron axons establish connections with target muscles forming branches of synaptic boutons, which are constantly added in order to maintain synaptic strength as the larva grows (Gramates and Budnik, 1999; Menon et al., 2013). Changes to bouton size and/or number are indicative of neurodevelopmental defects that are often observed in *Drosophila* models of NDDs (Bellosta and Soldano,

2019; Bodaleo and Gonzalez-Billault, 2016). To characterize the role of KDM5 at the synapse, we compared the NMJ structure in $kdm5^{140}$-null mutant animals to controls ($w^{1118}$). NMJs were visualized by immunolabeling third-instar larval NMJs with the neuronal membrane marker horseradish peroxidase (HRP) and the postsynaptic scaffold protein Discs large (Dlg), which is the *Drosophila* homolog of PSD95. We then quantified the number and size of type Ib synaptic boutons, which are predominantly responsible for muscle contraction (Newman et al., 2017), at muscle 4 of the third abdominal segment. Because $kdm5^{140}$ mutants show a slow-growth phenotype that results in larvae taking longer to develop to the same size as wild-type (WT) animals, we matched animals developmentally rather than chronologically, as we have done previously (Drelon et al., 2018, 2019). In addition, we normalized the number of boutons to muscle size to account for any slight differences in larval size. These analyses revealed that loss of *kdm5* alters NMJ morphology by decreasing the number and increasing the size of synaptic boutons (Figures 1A, 1B, 1F, and 1H).

To confirm the $kdm5^{140}$-null mutant phenotype and rule out the possibility that the altered larval growth rate of $kdm5^{140}$ animals indirectly caused the NMJ phenotypes observed, we used an inducible *kdm5* short hairpin RNA (shRNA) transgene (Chen et al., 2019; Liu and Secombe, 2015). Ubiquitous knockdown of *kdm5* using *Act5C-Gal4* reduced KDM5 protein levels by ~75%, which is not sufficient to delay larval growth in the same manner as the null allele (Figure S1). *kdm5* knockdown animals recapitulated the reduced NMJ bouton number phenotype that we observed in $kdm5^{140}$ larvae (Figures 1C, 1F, and 1H). Reducing *kdm5* also led to a modest increase in NMJ bouton size (p = 0.05) that was less pronounced but consistent with the $kdm5^{140}$-null phenotype. Combined, these data suggest that KDM5 is required to promote NMJ bouton number and to restrict bouton size.

Changes in bouton size correlate with changes in microtubule (MT) stability, which can be visualized by examining the distribution of the MT-binding protein Futsch (Nechipurenko and Broihier, 2012; Viquez et al., 2006). We therefore stained the NMJs of control and $kdm5^{140}$ animals with anti-Futsch and quantified the number of boutons containing unbundled MTs, which are characterized as looped or punctate staining (Packard et al., 2002). $kdm5^{140}$ mutant larvae displayed a higher proportion of boutons with unbundled MTs (punctate 24.6%, looped 9%) compared to controls (punctate 17.6%, looped 3.2%) (Figures 1J–1L). Thus, the increased proportion of unbundled MTs caused by loss of KDM5 may contribute to the increase in bouton size observed in these animals.

To determine where KDM5 function is required to mediate its effects on NMJ morphology, we restored *kdm5* expression in specific cell types within $kdm5^{140}$ protein-null animals. To do this, we used a *UAS-kdm5* transgene that drives low levels of expression (~2-fold increase over endogenous levels) (Drelon et al., 2019; Li et al., 2010; Secombe et al., 2007) and a range of well-characterized *Gal4* drivers. Re-expression of *kdm5* ubiquitously (*Act5C-Gal4* and *da-Gal4*), pan-neuronally (*elav-Gal4*), or in motor neurons (*OK6-Gal4*) significantly rescued the bouton number deficit of $kdm5^{140}$ larvae (Figures 1D and 1G). Restoring *kdm5* expression in muscles (*Mef2-Gal4*) or glia (*repo-Gal4*),
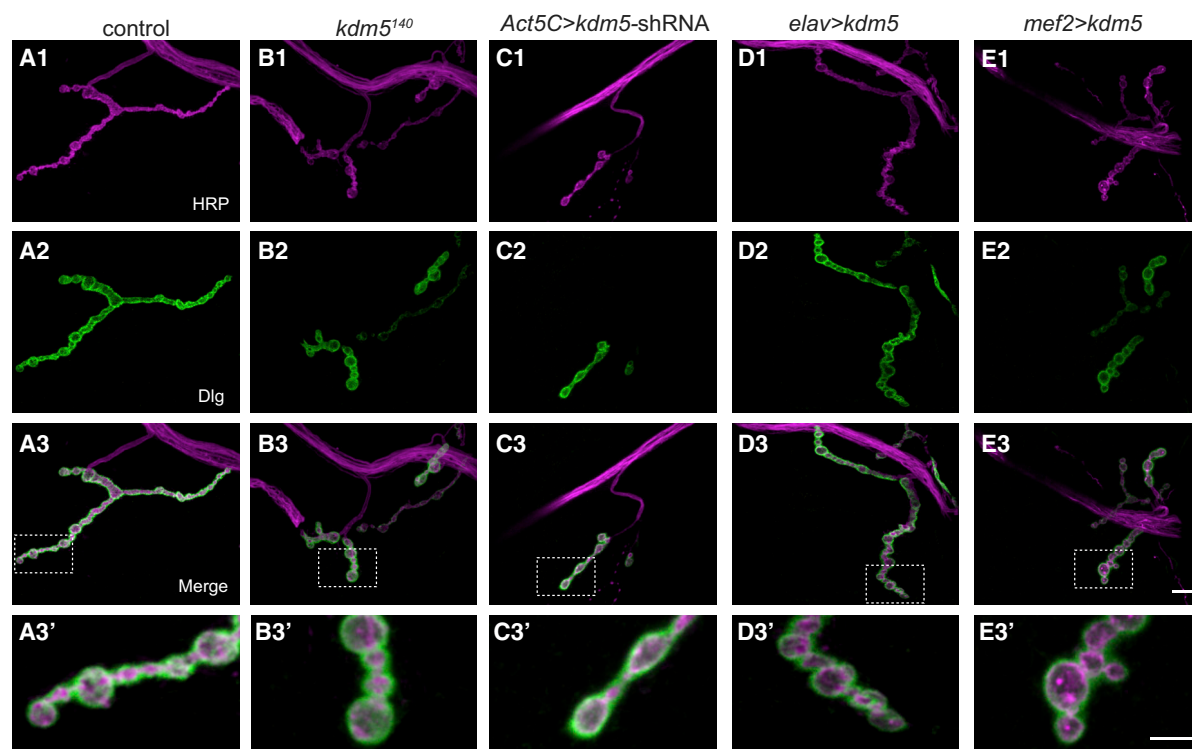
*kdm5^140* background
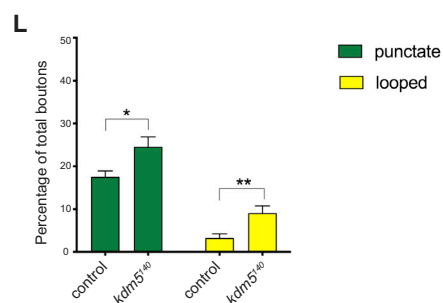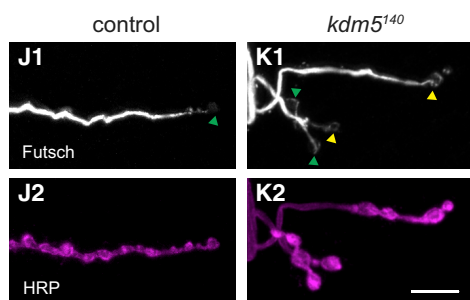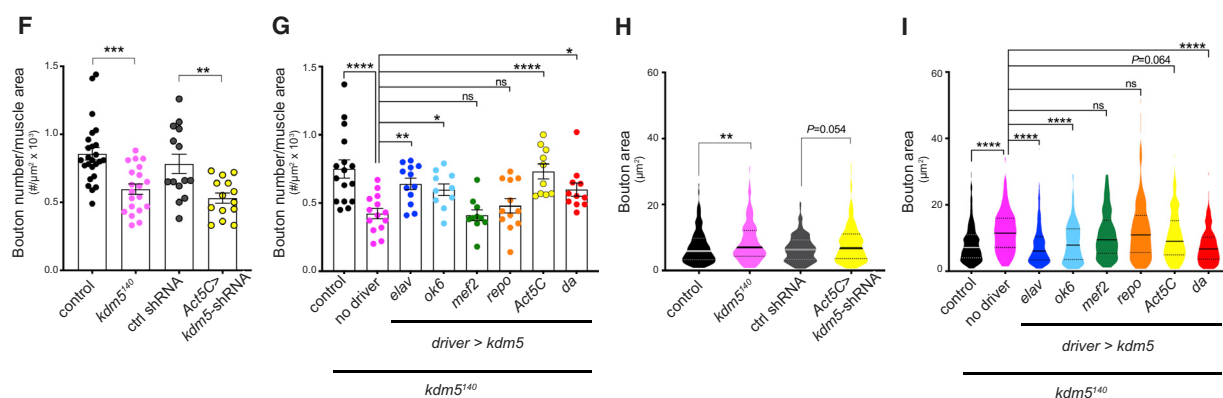


*(legend on next page)*

however, did not (Figures 1E and 1G). Similar findings were observed for bouton size phenotype in $kdm5^{140}$ larvae. Neuronal re-expression of $kdm5$ using $elav$-$Gal4$ and $OK6$-$Gal4$ restored bouton size similar to WT, whereas muscle or glial expression did not ($Mef2$-$Gal4$ and $repo$-$Gal4$, respectively) (Figure 1I). These data suggest that KDM5 impacts NMJ growth by regulating presynaptic gene expression.

### The JmjC domain and the C5HC2 motif of KDM5 are required for NMJ structure

Approximately half of the 122 reported NDD-associated variants in *KDM5A*, *KDM5B*, or *KDM5C* are predicted to compromise histone demethylase activity because they are expected to reduce or eliminate protein expression (Brookes et al., 2015; De Rubeis et al., 2014; Gonçalves et al., 2014; Najmabadi et al., 2011). We therefore examined the contribution of this chromatin-modifying activity to NMJ morphology using a fly strain with two point mutations in the JmjC domain that abolish enzymatic function ($kdm5^{JmjC*}$ allele) (Drelon et al., 2018; Navarro-Costa et al., 2016; Zamurrad et al., 2018) (Figure 2A). $kdm5^{JmjC*}$ homozygous larvae exhibited a decrease in bouton number but no change in bouton size compared to the isogenic control strain for this mutation ($kdm5^{WT}$) (Figures 2B–2E). Thus, the catalytic activity of KDM5 is required for only one of the phenotypes observed in the $kdm5$-null mutant, indicating that non-enzymatic activities are also required for proper NMJ structure.

To identify potential non-enzymatic means by which KDM5 could function in motor neurons, we surveyed known genetic alterations to human *KDM5* genes that are associated with ID. Interestingly, 29% of ID-associated missense variants in *KDM5C* occur within the helical region harboring the uncharacterized C5HC2 zinc-finger motif (Human Gene Mutation Database; HGMD) (Stenson et al., 2017), suggesting a key functional role for this domain. We therefore generated three fly strains harboring ID-associated mutations in the C5HC2 domain: $kdm5^{L854F}$, $kdm5^{R873W}$, and $kdm5^{Y874C}$, which are equivalent to

KDM5C (p.L731F), (p.R750W), and (p.Y751C), respectively (Figure 3A) (Jensen et al., 2005; Tzschach et al., 2006). These alleles were chosen because they result in moderate to severe ID, suggesting they may more dramatically change gene expression in neuronal lineages.

Similar to our approach for generating the $kdm5^{JmjC*}$ allele, we used a genomic rescue strategy to generate ID-associated alleles (Drelon et al., 2018; Li et al., 2010; Liu and Secombe, 2015; Navarro-Costa et al., 2016; Zamurrad et al., 2018). ID mutant fly strains lack the endogenous $kdm5$ locus and have the entire 11-kb $kdm5$ genomic region containing the point mutation and three tandem copies of the hemagglutinin (HA) epitope tag in an $attP$ site at cytological location 86F. The WT control strain for these alleles is homozygous for the $kdm5^{140}$ mutation and the HA-tagged WT locus at 86F ($kdm5^{WT}$) (Drelon et al., 2018; Zamurrad et al., 2018).

To determine whether the ID-associated alleles affected KDM5 protein levels, we performed a western blot using dissected larval CNS from $kdm5^{L854F}$, $kdm5^{R873W}$, or $kdm5^{Y874C}$ animals and found no change compared to $kdm5^{WT}$ (Figure 3B). Because a key feature of $kdm5^{140}$-null mutant larvae is slowed larval growth that delays pupariation, we quantified the developmental timing of $kdm5^{L854F}$, $kdm5^{R873W}$, and $kdm5^{Y874C}$ animals. Similar to our previous analyses of homozygous $kdm5^{JmjC*}$ animals (Drelon et al., 2018), ID mutant strains showed an identical developmental profile to $kdm5^{WT}$ (Figure 3D). Thus, we were able to examine the NMJ phenotypes of these animals without the complication of altered larval growth rate. All three ID-associated mutant fly strains were homozygous viable and visibly morphologically normal, although homozygous $kdm5^{R873W}$ and $kdm5^{Y874C}$ adult flies occurred slightly less frequently than expected (Figures 3E–3I). These alleles, therefore, do not dramatically alter the developmental functions of KDM5 that are required for adult viability.

Alleles of $kdm5$ that abolish enzymatic activity cause a global 2-fold increase in the ratio of H3K4me3 to total histone H3

---

**Figure 1. *kdm5* expression is required in motor neurons for normal NMJ development**

(A1–A3) NMJ morphology at muscle 4 of abdominal segment 3 (NMJ4-A3) of control ($w^{1118}$) third-instar larvae labeled with the presynaptic marker HRP (magenta; A1) and postsynaptic marker Dlg (green; A2), and merged (A3).

(B1–B3) $kdm5^{140}$ homozygous larva.

(C1–C3) $kdm5$ knockdown larva ($Act5C > kdm5$-$shRNA$).

(D1–D3) $kdm5^{140}$; $elav > UAS$-$kdm5$.

(E1–E3) $kdm5^{140}$; $mef2 > UAS$-$kdm5$.

(A3′–E3′) Boxed areas in (A3)–(E3) showing higher magnification of type Ib boutons. Scale bars, 10 μm (E3) and 5 μm (E3′).

(F) Quantification of type Ib bouton number normalized to muscle surface area. ***p = 0.0001, **p = 0.0041. Control ($w^{1118}$) n = 25, $kdm5^{140}$ n = 20, $Act5C > kdm5$-$shRNA$ n = 14, control (+; shRNA) n = 14. Error bars: mean ± SEM

(G) Quantification of type Ib bouton number normalized to muscle surface area. ****p < 0.0001, **p = 0.0029, *p = 0.0036 ($OK6$), *p = 0.0282 ($da$); ns, not significant. Control ($w^{1118}$) n = 16, no driver ($kdm5^{140}$; $UAS$-$kdm5$) n = 14, $kdm5^{140}$; $elav > kdm5$ n = 12, $kdm5^{140}$; $OK6 > kdm5$ n = 10, $kdm5^{140}$; $mef2 > kdm5$ n = 10, $kdm5^{140}$; $repo > kdm5$ n = 12, $kdm5^{140}$; $Act5C > kdm5$ n = 10, $kdm5^{140}$; $da > kdm5$ n = 11. Error bars: mean ± SEM

(H) Quantification of type Ib bouton size in $kdm5^{140}$ larvae and ubiquitous knockdown ($Act5C > kdm5$-$shRNA$). Violin plots show the frequency distribution of bouton surface area indicating the median and quartiles. **p = 0.0020. Control ($w^{1118}$) n = 327, $kdm5^{140}$ n = 280, $Act5C > kdm5$-$shRNA$ n = 198, control (+; shRNA) n = 281.

(I) Quantification of type Ib bouton size in rescue experiments using the genotypes shown. ****p < 0.0001, p = 0.064. Control ($w^{1118}$) n = 340, no driver ($kdm5^{140}$; $UAS.kdm5$) n = 149, $kdm5^{140}$; $elav > kdm5$ n = 245, $kdm5^{140}$; $OK6 > kdm5$ n = 191, $kdm5^{140}$; $mef2 > kdm5$ n = 123, $kdm5^{140}$; $repo > kdm5$ n = 254, $kdm5^{140}$; $Act5C > kdm5$ n = 181, $kdm5^{140}$; $da > kdm5$ n = 201.

(J1–K2) Futsch (white) immunolabeling in segments of NMJ4-A3 showing microtubules within synaptic boutons and HRP (magenta) from control (J1 and J2) and $kdm5^{140}$ (K1 and K2). Green triangles indicate punctate signal and yellow triangles indicate looped boutons. Scale bar, 10 μm.

(L) Quantification of unbundled boutons, punctate and looped, as the percentage of total boutons in NMJ4-A3 of control and $kdm5^{140}$. *p = 0.0137, **p = 0.0047. Control n = 20, $kdm5^{140}$ n = 21. Error bars: mean ± SEM
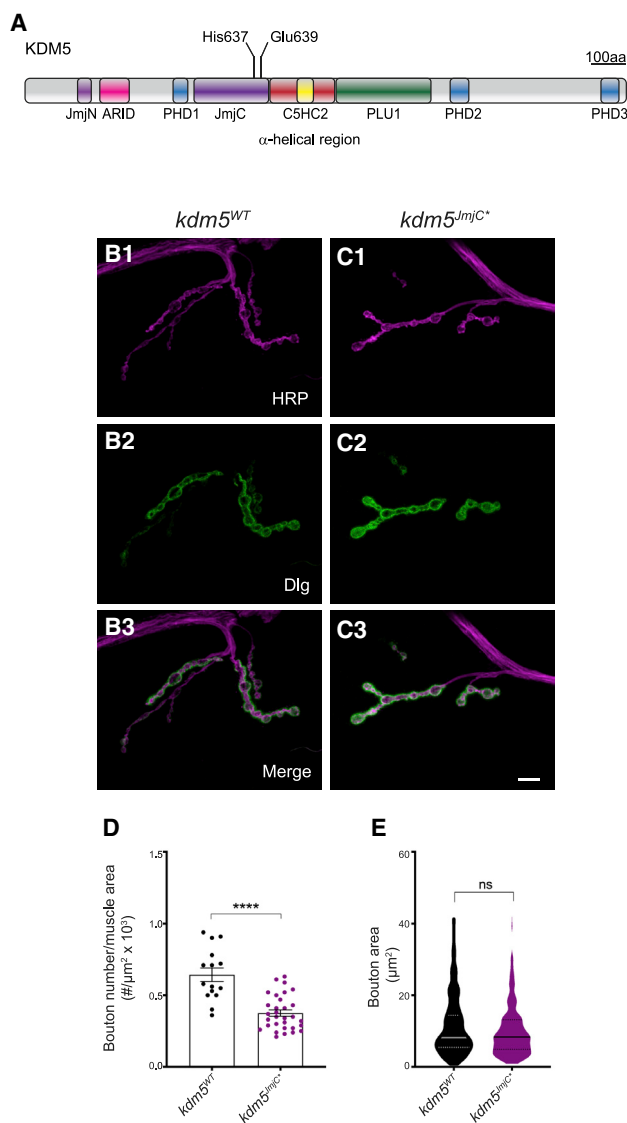
**Figure 2. The demethylase activity of KDM5 is required to regulate NMJ bouton number**

(A) Schematic of *Drosophila* KDM5 showing the position of the mutations in the JmjC domain that abolish enzymatic activity.

(B1–C3) NMJ4-A3 of wild-type (*kdm5^WT^*; B1–B3) and demethylase-inactive (*kdm5^JmjC*^*; C1–C3) third-instar larvae stained with HRP (B1 and C1) and Dlg (B2 and C2), and merged (B3 and C3). Scale bar, 10 μm.

(D) Quantification of type Ib bouton number normalized to muscle surface area in *kdm5^WT^* and *kdm5^JmjC*^*. ****p < 0.0001. *kdm5^WT^* n = 15, *kdm5^JmjC*^* n = 31. Error bars: mean ± SEM

(E) Quantification of type Ib bouton size in *kdm5^WT^* and *kdm5^JmjC*^*. *kdm5^WT^* n = 234, *kdm5^JmjC*^* n = 388. ns, not significant.

(Drelon et al., 2018; Navarro-Costa et al., 2016; Secombe et al., 2007; Zamurrad et al., 2018). To examine the effect of the KDM5^L854F^, KDM5^R873W^, and KDM5^Y874C^ mutations on histone demethylase activity *in vivo*, we similarly quantified levels of H3K4me3 using dissected larval CNS tissue. In contrast to *kdm5^JmjC*^*, *kdm5^L854F^*, *kdm5^R873W^*, and *kdm5^Y874C^* did not affect H3K4me3 levels compared to total histone H3 (Figures 3B and

3C). Although it remains possible that these mutations have modest or gene-specific effects that are undetectable by western blot, these alleles do not abolish demethylase activity *in vivo*.

To further characterize these ID-associated mutations, we examined their thermodynamic effect on KDM5 using the web server DynaMut, which calculates the change in folding Gibbs free energy (ΔΔG) by combining normal-mode analysis and graph-based signatures. We also used DynaMut to measure the vibrational entropy (ΔΔSvib), a measure of molecule flexibility (Rodrigues et al., 2018). Because there is no crystal structure of *Drosophila* KDM5, we analyzed the KDM5A structure PDB: 5CEH, which covers a broader N-terminal region and C-terminal helical zinc-binding domain compared to the structures available for KDM5C (Vinogradova et al., 2016) (Figure S2A). All residues investigated are conserved between *Drosophila* KDM5, human KDM5A, and human KDM5C. All three mutations were predicted to thermodynamically stabilize the protein with the maximum effect shown by Y720C (Y874C in *Drosophila*) (ΔΔG: 1.759 kcal/mol), followed by L700F (L854F in *Drosophila*) (ΔΔG: 1.624 kcal/mol) (Figures S2B–S2D). The latter is predicted to generate new hydrophobic contacts with residues localized in the adjacent helix and increase hydrogen bonds with a residue inside the first zinc-binding site (Figure S2B). DynaMut also predicted the greatest decrease in molecule flexibility for L700F/L854F using the Elastic Network Contact Model (ΔΔSvib ENCoM: −5.152 kcal·mol⁻¹·K⁻¹). These results, together with the position of the L700/L854 residue in the middle of the first zinc-binding site, suggest that this amino acid change may have the most dramatic impact on KDM5 function compared to the other amino acid substitutions (Figure S2A).

To determine the effect of *kdm5^L854F^*, *kdm5^R873W^*, and *kdm5^Y874C^* on NMJ morphology, we quantified type Ib synaptic bouton number and size in homozygous mutant larvae. *kdm5^L854F^* larvae had significantly fewer muscle 4 synaptic boutons compared to *kdm5^WT^*. In contrast, *kdm5^Y874C^* animals exhibited a mild reduction (p = 0.077) whereas *kdm5^R873W^* bouton number was indistinguishable from *kdm5^WT^* animals (Figures 4A–4E). We additionally found an increase in *kdm5^L854F^* bouton size whereas *kdm5^R873W^* or *kdm5^Y874C^* mutants were unaffected compared to *kdm5^WT^* (Figure 4F). Based on our observation that *kdm5^140^* mutant larvae show a change in MT dynamics (Figures 1J–4L), we carried out anti-Futsch staining of the two mutants that showed morphological NMJ phenotypes, *kdm5^L854F^* and *kdm5^JmjC*^*. *kdm5^L854F^* mutant larvae showed a higher proportion of boutons with looped MTs compared to *kdm5^WT^* (36.6% versus 15.7%, respectively). In contrast, no difference was observed in the proportion of boutons with unbundled MTs in *kdm5^JmjC*^* animals (Figures 4G–4J). Together, our analyses of Futsch staining in *kdm5^140^*, *kdm5^L854F^*, and *kdm5^JmjC*^* mutants suggest a link between increased bouton size and altered MT dynamics at the synapse. In addition, these data suggest a key role for the C5HC2 motif, but not the JmjC domain, in this process.

## Mutations in the JmjC domain and the C5HC2 motif of KDM5 show distinct effects on NMJ function

Because the *kdm5^JmjC*^* demethylase-dead strain and the *kdm5^L854F^* ID mutant showed NMJ phenotypes without altering
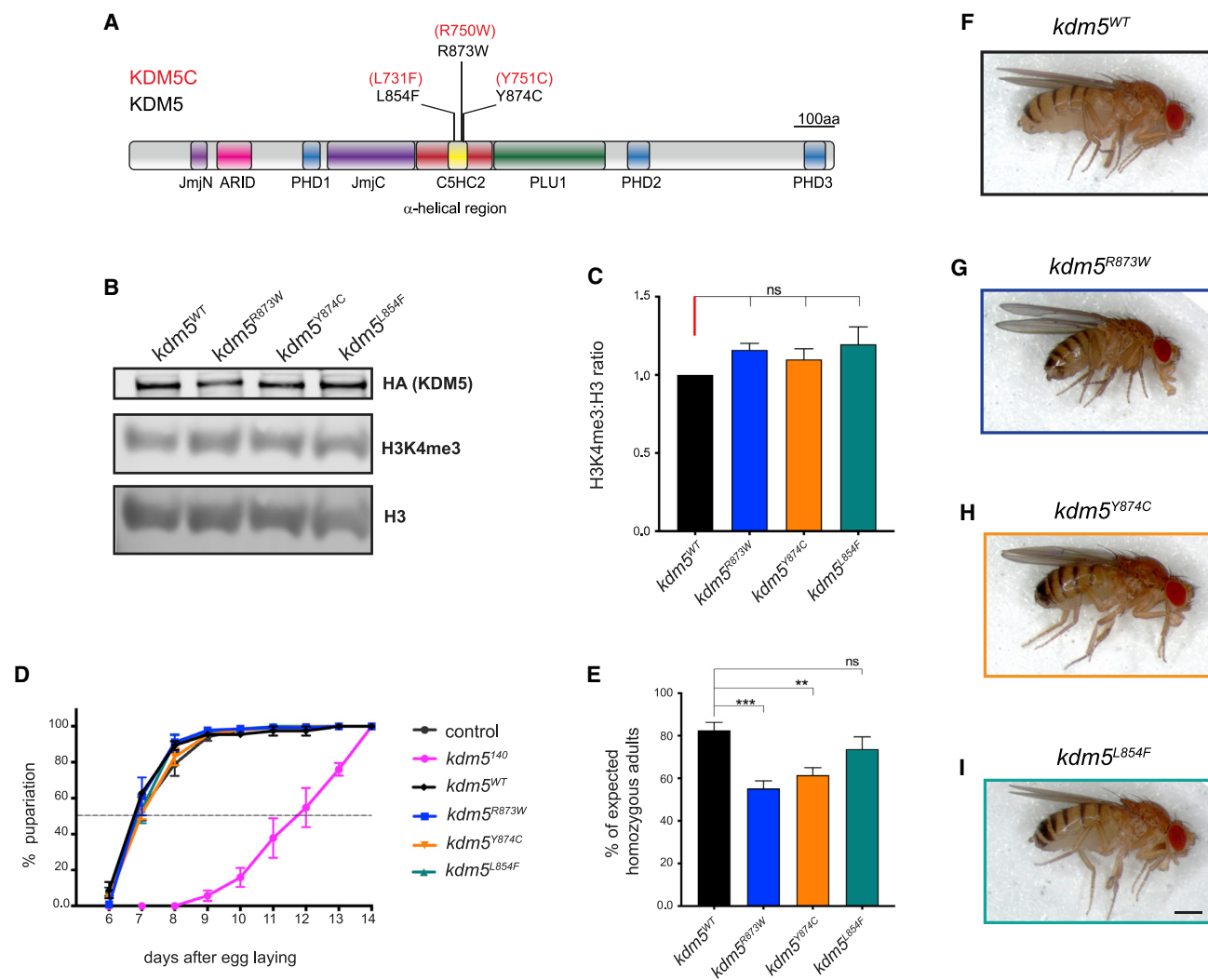
**Figure 3. Fly strains harboring ID-associated mutations are viable and developmentally similar to controls**

(A) Schematic of *Drosophila* KDM5 showing missense mutations that are equivalent ID-associated variants in human KDM5C.

(B) Western blot of larval CNS from *kdm5^WT^*, *kdm5^R873W^*, *kdm5^Y874C^*, and *kdm5^L854F^* showing expression of HA-tagged KDM5 (top), H3K4me3 (middle), and total histone H3 (bottom).

(C) Triplicate quantification of H3K4me3 levels relative to total histone H3 in *kdm5^R873W^*, *kdm5^Y874C^*, and *kdm5^L854F^* compared to the ratio observed in *kdm5^WT^*. ns, not significant. Error bars: mean ± SEM

(D) Developmental timing of control (*w^1118^*), *kdm5^WT^*, *kdm5^140^*, *kdm5^R873W^*, *kdm5^Y874C^*, and *kdm5^L854F^*. The dashed line indicates 50% pupariation. Control n = 88, *kdm5^140^* n = 52, *kdm5^WT^* n = 398, *kdm5^R873W^* n = 216, *kdm5^Y874C^* n = 294, *kdm5^L854F^* n = 137. Error bars: SEM

(E) Adult survival of homozygous *kdm5^WT^*, *kdm5^R873W^*, *kdm5^Y874C^*, and *kdm5^L854^* adult flies from intercrossed heterozygous parents as a percentage of the number expected based on Mendelian expectations. ***p = 0.0001, **p = 0.0057. Total scored flies: *kdm5^WT^* n = 359, *kdm5^R873W^* n = 1,164, *kdm5^Y874C^* n = 1,193, *kdm5^L854F^* n = 544. Error bars: mean ± SEM

(F–I) *kdm5^WT^* (F), *kdm5^R873W^* (G), *kdm5^Y874C^* (H), and *kdm5^L854F^* (I) female flies. Scale bar, 50 μm.

larval growth rate, we chose to focus further analyses on these two strains. In addition, *kdm5^L854F^* does not increase global levels of H3K4me3 (Figures 3B and 3C) and its NMJ phenotypes were not identical to the demethylase-dead *kdm5^JmjC*^*. Comparing these two strains therefore allows us to examine KDM5's demethylase activity-dependent and independent functions at the NMJ. To test whether the structural defects observed in *kdm5^JmjC*^* and *kdm5^L854F^* were associated with larval movement deficits, we quantified the crawling behavior of mutant third-instar larvae

compared to control *kdm5^WT^* (Kashima et al., 2017; Li et al., 2007). There was a significant decrease in locomotor performance, as both genotypes traveled a shorter total distance (path length) compared to *kdm5^WT^* (Figures 5A and 5E). The shorter distance traveled was likely due to reduced locomotor speed as *kdm5^JmjC*^* and *kdm5^L854F^* animals showed lower average and maximal velocities as well as average speed normalized to larval size (Figures 5B–5D). Disrupting the function of the JmjC domain or the C5HC2 motif therefore affects functional motor outputs.
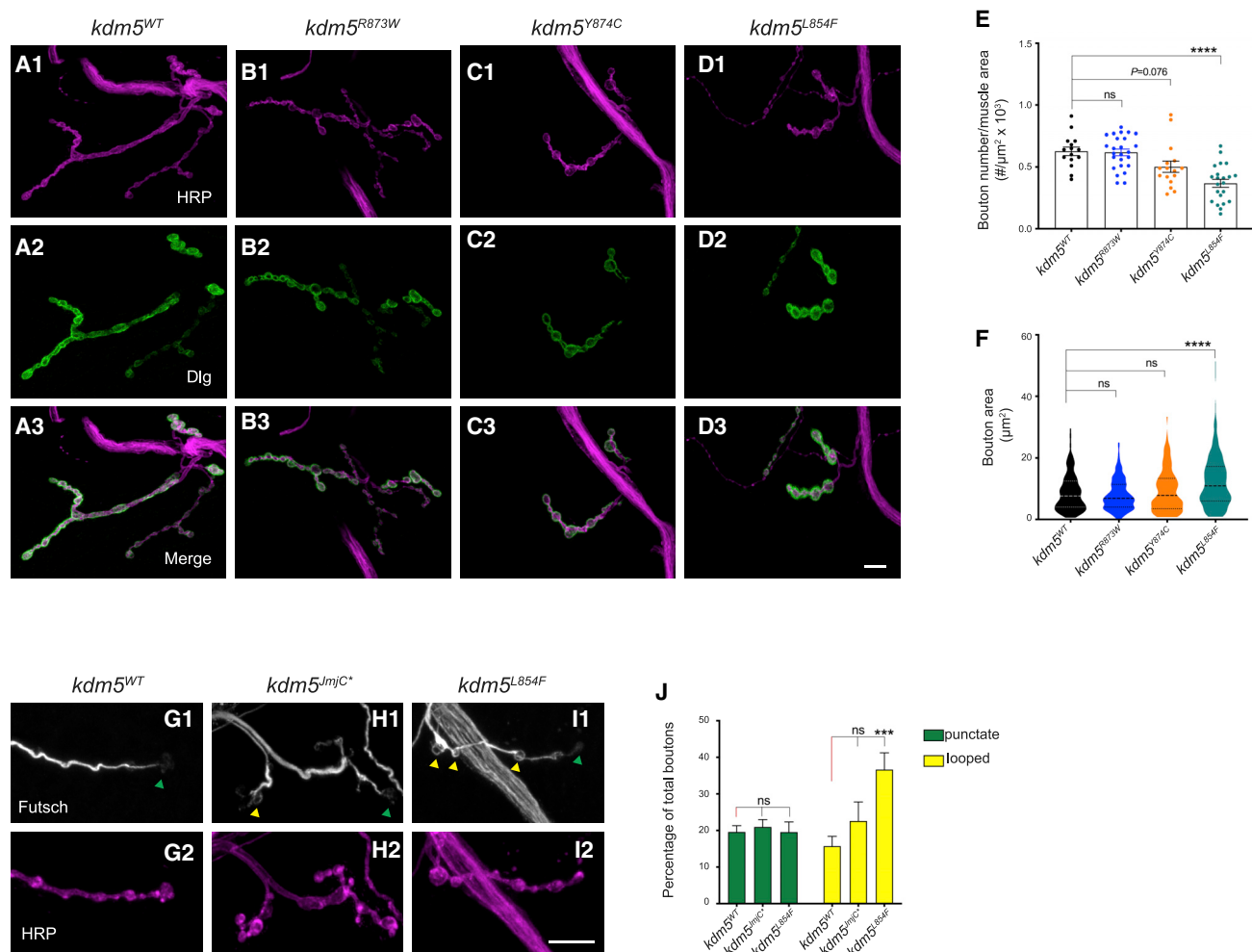
**Figure 4. The L854F mutation in the C5HC2 domain of KDM5 affects NMJ bouton size and number**

(A1–D3) NMJ morphology at muscle 4-A3 of third-instar larvae labeled with HRP (magenta; A1, B1, C1, and D1) and Dlg (green; A2, B2, C2, and D2), and merged (A3, B3, C3, and D3).

(A1–A3) $kdm5^{WT}$.

(B1–B3) $kdm5^{R873W}$.

(C1–CC3) $kdm5^{Y874C}$.

(D1–D3) $kdm5^{L854F}$. Scale bar, 10 μm.

(E) Quantification of type Ib bouton number normalized to muscle surface area from $kdm5^{WT}$, $kdm5^{R873W}$, $kdm5^{Y874C}$, and $kdm5^{L854}$ larvae. ****p < 0.0001. $kdm5^{WT}$ n = 15, $kdm5^{R873W}$ n = 25, $kdm5^{Y874C}$ n = 16, $kdm5^{L854F}$ n = 22. ns, not significant. Error bars: mean ± SEM

(F) Quantification of type Ib bouton size from $kdm5^{WT}$, $kdm5^{R873W}$, $kdm5^{Y874C}$, and $kdm5^{L854}$ larvae. ****p<0.0001. $kdm5^{WT}$ n = 309, $kdm5^{R873W}$ n = 214, $kdm5^{Y874C}$ n = 97, $kdm5^{L854F}$ n = 176.

(G–I) Futsch (white) immunolabeling and HRP (magenta) in NMJ4-A3 from $kdm5^{WT}$ (G1 and G2), $kdm5^{JmjC*}$ (H1 and H2), and $kdm5^{L854}$ (I1 and I2) larvae. Green triangles indicate boutons with punctate signal and yellow triangles indicate looped boutons. Scale bar, 10 μm.

(J) Quantification of unbundled boutons, punctate (green) and looped (yellow), as the percentage of total boutons in NMJ4-A3 of $kdm5^{WT}$, $kdm5^{JmjC*}$, and $kdm5^{L854}$ larvae. ***p = 0.0007. $kdm5^{WT}$ n = 19, $kdm5^{JmjC*}$ = 12, $kdm5^{L854F}$ n = 14. Error bars: mean ± SEM

To directly measure neuronal activity in $kdm5^{JmjC*}$ and $kdm5^{L854F}$ mutants, we examined evoked and spontaneous synaptic transmission at the glutamatergic NMJ of larval muscle 6, which displayed similar bouton phenotypes to those observed in muscle 4 (Figure S3). Compared to $kdm5^{WT}$, evoked excitatory junctional currents (eEJCs) were reduced in $kdm5^{JmjC*}$ but not in $kdm5^{L854F}$ larvae (Figures 5F and 5G). The impaired neurotransmission observed in $kdm5^{JmjC*}$ animals could be caused by defects in synaptic excitation, neurotransmitter release, or postsynaptic response. Analyses of miniature excitatory junctional current (mEJC) amplitudes did not show any differences between $kdm5^{JmjC*}$ and $kdm5^{WT}$ animals (Figure 5H). These data suggest that the reduction in eEJCs was caused by neither a defect in the response of postsynaptic glutamatergic receptors to glutamate nor the amount of glutamate released by a single vesicle. mEJC frequency in
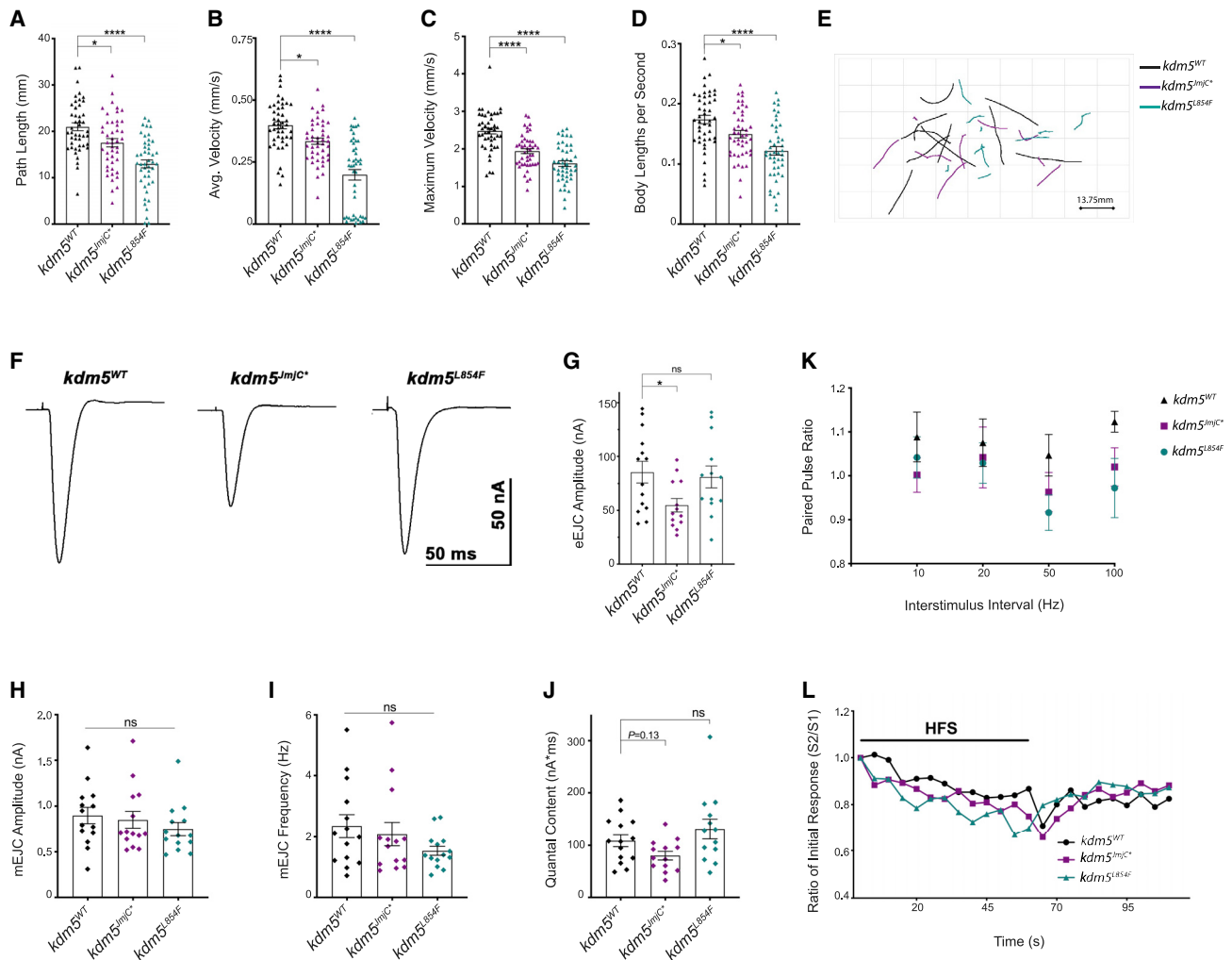
**Figure 5. KDM5 mutations in the JmjC and C5HC2 domains affect larval locomotion**

(A–E) Movement of third-instar $kdm5^{WT}$, $kdm5^{JmjC*}$, and $kdm5^{L854F}$ larvae. $kdm5^{WT}$ n = 45, $kdm5^{JmjC*}$ n = 45, $kdm5^{L854F}$ n = 45.

(A) Traveled distance. *p = 0.0114, ****p < 0.0001. Error bars: mean ± SEM

(B) Average speed. *p = 0.0105, ****p < 0.0001. Error bars: mean ± SEM

(C) Maximum speed. ****p < 0.0001. Error bars: mean ± SEM

(D) Average speed normalized to larval size. *p = 0.0248, ****p < 0.0001. Error bars: mean ± SEM

(E) Representative path trajectories of 10 larvae from each genotype.

(F) Representative evoked excitatory junctional currents (eEJCs) recorded from muscle 6 in $kdm5^{WT}$, $kdm5^{JmjC*}$, and $kdm5^{L854F}$ larvae.

(G) Quantification of eEJC amplitudes. *p = 0.0368; ns, not significant. Error bars: mean ± SEM

(H and I) Quantification of miniature excitatory junctional current (mEJC) amplitude (H) and frequency (I). Error bars: mean ± SEM
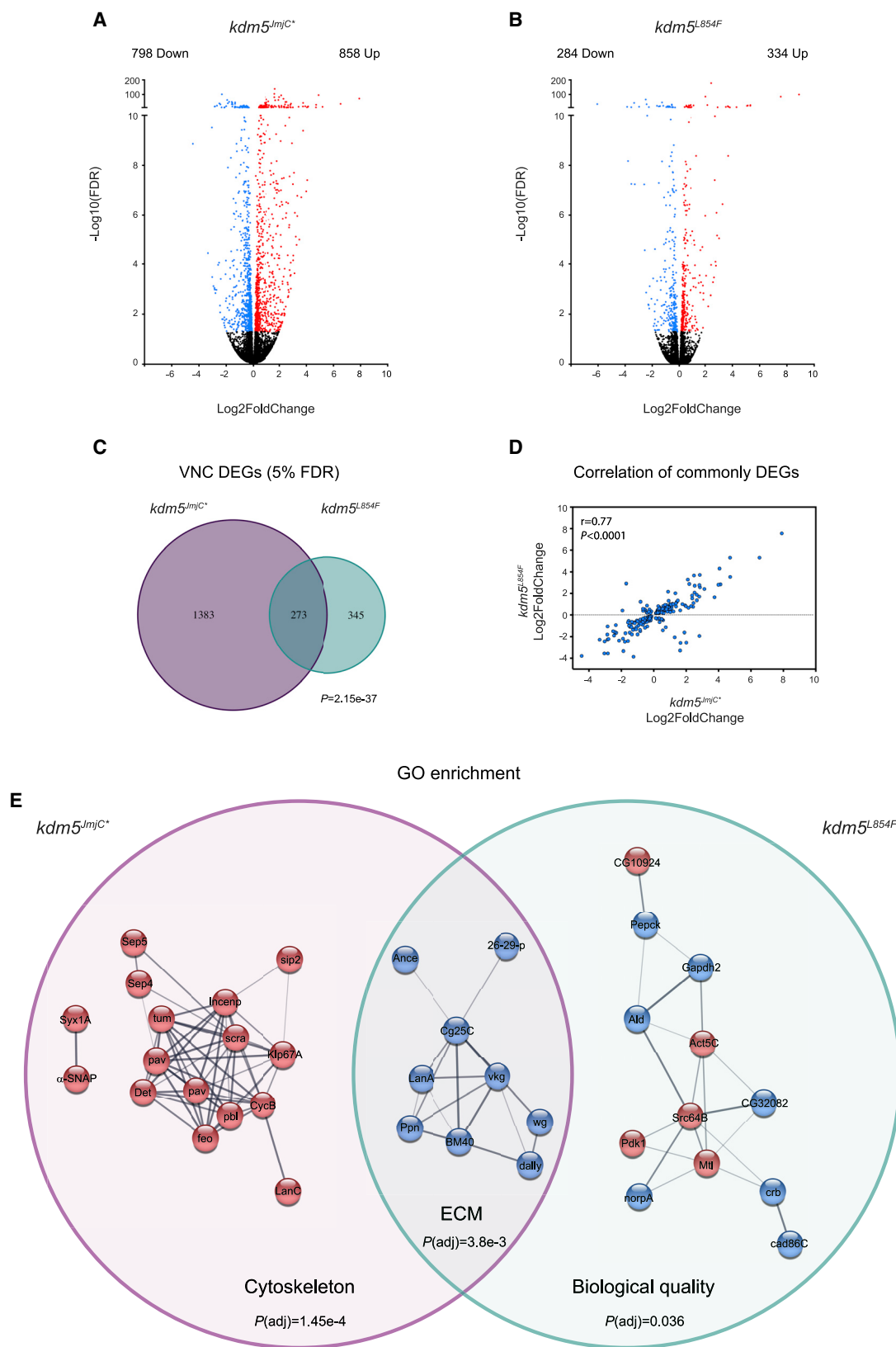
(J) Quantification of quantal content (eEJC area (nA*ms)/mEJC area (nA*ms)).Error bars: mean ± SEM

(K) Paired-pulse ratio (eEJC amplitude second response/eEJC amplitude first response) across multiple interstimulus intervals. Error bars: SEM

(L) eEJC amplitudes, normalized to the first response, during HFS (20 Hz × 60 s) followed by a recovery period of stimulation (0.2 Hz × 50 s). $kdm5^{WT}$ n = 12, $kdm5^{JmjC}$ n = 14, $kdm5^{L854F}$ n = 13. Error bars representing SEM are not displayed here to facilitate visualization.

$kdm5^{JmjC*}$ mutant larvae was also unaltered compared to $kdm5^{WT}$, indicating that there were no changes in the number of functional active release sites (Figure 5I) (Long et al., 2010). Furthermore, immunohistochemical analysis of $kdm5^{JmjC*}$ NMJs with an antibody to Bruchpilot (Brp) revealed that active zones show no changes in density or defects in apposition to postsynaptic glutamatergic receptors (GluRIIC) relative to $kdm5^{WT}$ (Figures S3F and S3G). We also examined quantal content (ratio of eEJC area/mEJC area), which reflects the

number of vesicles released per stimulus, and observed a slight decrease in $kdm5^{JmjC*}$ larvae compared to $kdm5^{WT}$ (p = 0.13) (Figure 5J). $kdm5^{L854F}$ mutant larvae did not show any differences in mEJC amplitude or frequency, quantal content, or active zone density or apposition (Figures 5 and S3). Taken together, these data indicate that loss of demethylase activity and the ID-associated mutation in the C5HC2 domain similarly impairs larval locomotion but only loss of demethylase activity reduces eEJC amplitudes.

**A** $kdm5^{JmjC*}$

798 Down    858 Up

**B** $kdm5^{L854F}$

284 Down    334 Up

**C** VNC DEGs (5% FDR)

$kdm5^{JmjC*}$    $kdm5^{L854F}$

1383    273    345

$P$=2.15e-37

**D** Correlation of commonly DEGs

r=0.77
$P$<0.0001

$kdm5^{L854F}$ Log2FoldChange

$kdm5^{JmjC*}$ Log2FoldChange

**E** GO enrichment

$kdm5^{JmjC*}$    $kdm5^{L854F}$

ECM
$P$(adj)=3.8e-3

Cytoskeleton
$P$(adj)=1.45e-4

Biological quality
$P$(adj)=0.036

*(legend on next page)*

To evaluate whether the deficiency in neurotransmission observed in kdm5[JmjC*] mutants was due to differences in synaptic vesicle release probability, we analyzed the responses to paired-pulse stimuli given at variable intervals (Figure 5K). The paired-pulse ratio (PPR), calculated by dividing the eEJC of the second response by the first, did not exhibit differences at any interstimulus interval for kdm5[JmjC*] or kdm5[L854F] mutants compared to kdm5[WT] control larvae. We also assessed the dynamics of synaptic vesicle recycling by recording eEJCs during a period of high-frequency stimulation (HFS) (20 Hz × 60 s) followed by a recovery period (0.2 Hz × 50 s) (Long et al., 2010). Similar to kdm5[WT], both mutants showed a decrease in eEJCs during HFS, when the pool of readily releasable vesicles is depleted, and an increase in eEJCs during the recovery period when the pool is replenished (Figure 5L). Together, these data show that the reduction in eEJC amplitudes caused by loss of demethylase activity was not likely the result of perturbations in vesicle release probability nor endocytic recycling.

## Mutations in KDM5 that affect NMJ structure alter transcriptional programs in the VNC

KDM5 is likely to exert its effect on synaptic structure and function by regulating gene expression. Because KDM5 functions presynaptically to regulate bouton number and size (Figure 1), we conducted transcriptomic analyses of dissected VNCs where the soma of motor neurons reside. Quadruplicate RNA-seq from kdm5[JmjC*] and kdm5[L854F] mutant larvae revealed that both mutations alter gene expression relative to kdm5[WT]. Using a false discovery rate (FDR) cutoff of 5%, kdm5[JmjC*] mutants showed 1,656 differentially expressed genes (DEGs), 858 of which were upregulated and 798 of which were downregulated (Figure 6A; Table S1). The kdm5[L854F] allele also altered gene expression, although fewer genes were differentially expressed than in kdm5[JmjC*], with 284 downregulated and 334 upregulated genes relative to kdm5[WT] (5% FDR) (Figure 6B; Table S2). Comparing the genes that were dysregulated in the two genotypes uncovered a significant number of genes that were dysregulated by both alleles (273; p = 2.15e-37) in addition to many genes that were uniquely altered in either kdm5[JmjC*] or kdm5[L854F] (Figure 6C). There was a strong correlation between commonly dysregulated genes, 242 of which behaved similarly in the two genotypes (r = 0.77; Figure 6D), suggesting that these two mutations affect one or more KDM5 functions required at a subset of target genes. KDM5 therefore uses both its demethylase and its C5HC2 zinc-finger activity to regulate presynaptic expression programs.

Similar to previous studies of KDM5 in *Drosophila* and other species (Chen et al., 2019; Drelon et al., 2018; Iwase et al., 2017; Mariani et al., 2016; Scandaglia et al., 2017; Zamurrad et al., 2018), the changes in gene expression in the VNCs of

kdm5[JmjC*] and kdm5[L854F] mutants were modest, averaging ~2-fold (Figures 6A and 6B). KDM5 is therefore likely to function in motor neurons by regulating sets of target genes within critical pathways, which can be highlighted by interrogating Gene Ontology (GO) and protein-interaction pathway databases. Examining genes that were dysregulated only in kdm5[JmjC*] revealed an enrichment for the GO cellular component category of cytoskeleton (P(adj) = 1.45e-4) (Figure 6E). All genes within this group were upregulated, consistent with the canonical function of the demethylase activity of KDM5 in transcriptional repression. Interestingly, in addition to well-characterized roles during mitosis, many of these genes play additional roles in post-mitotic neurons, particularly in the regulation of synaptic function. For example, genes encoding the septin proteins Septin4 and Septin5 and the synaptic SNARE complex component α-SNAP, upregulated in kdm5[JmjC*] mutant CNS, are all linked to the negative regulation of neurotransmitter release (Brunger et al., 2019; Marttinen et al., 2015). This observation is in keeping with the electrophysiological defect observed in kdm5[JmjC*] mutant larvae, which showed a slight decrease in the number of vesicles being released (quantal content; Figure 5J).

Similar GO analyses of the genes that were dysregulated in both kdm5[JmjC*] and kdm5[L854F] mutant VNCs identified a single enriched category of extracellular matrix (ECM) organization (P(adj) = 3.8e-3). All of the genes in this category, which encode proteins that function in the extracellular space, showed reduced expression compared to kdm5[WT], implicating KDM5 in their activation. This included components of the basement membrane such as laminin A (lanA), collagen type IV alpha 1 (col4α1/Cg25c), and Viking (Vkg) (collagen IV), which form a complex (Guruharsha et al., 2011) (Figure 6E). In addition to playing structural roles, these proteins contribute to signaling, as emphasized by the presence of the Wnt/Wg pathway ligand Wingless, a well-established regulator of NMJ bouton growth, within this network (Figure 6E) (Packard et al., 2002). We also examined the 345 genes that were uniquely altered in kdm5[L854F] mutants and found a single enriched GO category of regulation of biological quality (P(adj) = 0.036) that comprised a combination of up- and downregulated genes that modulate qualitative or quantitative traits (Figure 6E). This group included proteins that influence synaptic bouton size such as phosphoinositide-dependent kinase 1 (Pdk1) (Cheng et al., 2011). In addition, genes encoding proteins that interact with, or regulate, the microtubule and actin cytoskeletons such as the Rac family protein Mtl (Hakeda-Suzuki et al., 2002; Trogden and Rogers, 2015) and the kinase Src64B (Feuillette et al., 2020) were dysregulated (Figure 6E; Table S2). Combined, these RNA-seq data provide molecular insights into potential mechanisms by which KDM5 carries out its neuromorphological and synaptic functions (Figure 7).

---

**Figure 6. kdm5[JmjC*] and kdm5[L854F] affect gene expression programs in the larval VNC**

(A and B) Volcano plots showing dysregulated genes (5% FDR; red) in the VNC of kdm5[JmjC*] (A) and kdm5[L854F] (B).

(C) Venn diagram showing overlap between kdm5[JmjC*] and kdm5[L854F] RNA-seq data. p = 2.15e-37.

(D) Correlation between overlapping dysregulated genes from kdm5[L854F] and kdm5[JmjC*].

(E) Networks from enriched GO categories affected in kdm5[JmjC*] (GO:0005856), kdm5[JmjC*] and kdm5[L854F] (GO:0005576), and kdm5[L854F] (GO:0065008). Red color indicates upregulation and blue indicates downregulation compared to kdm5[WT].

See also Tables S1 and S2.

Larval brain



NMJ structure

Glutamatergic
neurotransmission

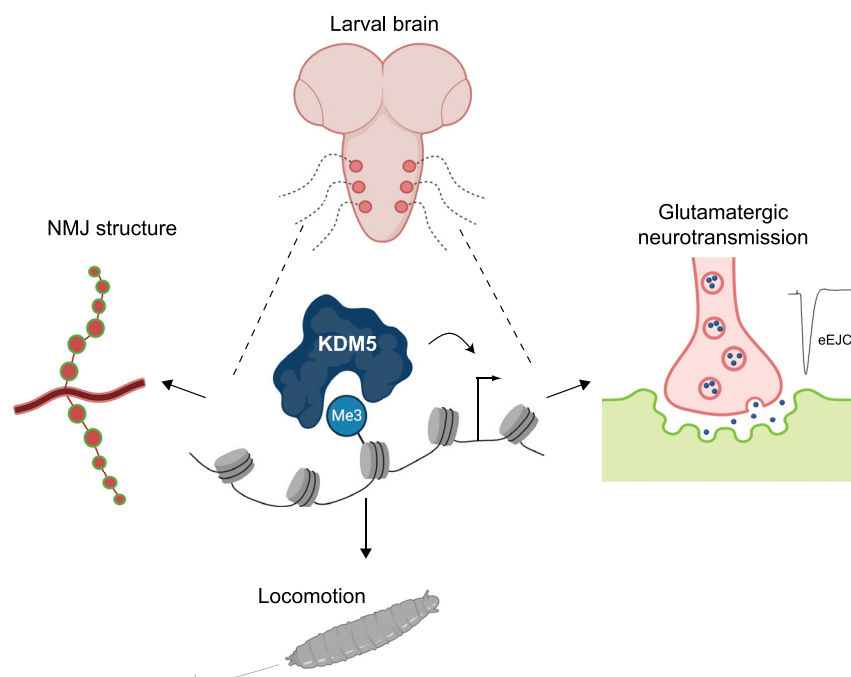KDM5

Me3

eEJC

Locomotion

**Figure 7. Model of KDM5 function at the NMJ**

KDM5 regulates gene expression programs in motor neurons that are required for normal morphology and synaptic function of the NMJ.

## DISCUSSION

Mutations in three of the four *KDM5* paralogs in humans are associated with NDDs, suggesting that these proteins are key contributors to neuronal development and/or function. The roles that KDM5 proteins play in regulating synaptic function, however, remain largely uncharacterized. Here we show that KDM5 regulates the expression of genes within the motor neuron that are required for the growth and function of the *Drosophila* larval NMJ. This synapse serves as a model for mammalian CNS glutamatergic synapses (Coll-Tané et al., 2019; Koh et al., 2000; Menon et al., 2013), which are altered in a number of inherited forms of cognitive impairment, including fragile X syndrome, Angelman syndrome, and Rett syndrome (Volk et al., 2015). Our experiments demonstrate that the mutations in different domains of KDM5 can cause both overlapping and distinct morphological and functional phenotypes at the NMJ. This is likely to be, at least partially, due to the JmjC and C5HC2 domains facilitating both shared and unique aspects of gene regulation in the larval VNC. Combined, our data lead us to propose that KDM5 uses several distinct gene-regulatory functions in NMJ glutamatergic neurons to influence functional and structural neuronal characteristics.

Our analyses establish the importance of the histone demethylase activity of KDM5 at the larval NMJ, providing further support for the model that loss of enzymatic activity contributes to the cognitive phenotypes observed in patients with mutations in *KDM5* genes. The $kdm5^{JmjC*}$ fly strain, but not the ID allele $kdm5^{L854F}$, exhibited an evoked neurotransmission defect that correlated with a mild deficit in the number of vesicles being released per stimulus. The demethylase activity of KDM5 is therefore needed for appropriate glutamatergic neurotransmission.

Although this allele is not a patient-associated mutation, at least half of the known ID-associated variants in *KDM5* family genes are expected to affect histone demethylase activity (Brookes et al., 2015; Lebrun et al., 2018). Thus, phenotypic analyses of this allele are likely to have implications for a number of patients. Based on our analyses of genes that were dysregulated only in the VNC of $kdm5^{JmjC*}$ mutant larvae, we propose that the upregulation of cytoskeletal genes that negatively regulate presynaptic neurotransmitter release plays a key role in the eEJC phenotype observed. For example, the α-*SNAP* gene has an evolutionarily conserved function in the inhibition of synaptic vesicle fusion through its interaction with the SNARE complex component syntaxin (Brunger et al., 2019). The expression of genes encoding the GTP-binding septins (Septin4 and Septin5), which can also impact vesicle release, was also upregulated in $kdm5^{JmjC*}$. One of the mammalian paralogs of Septin4 can inhibit synaptic vesicle release by forming a filament barrier (Yang et al., 2010) and, like α-SNAP, can interact with syntaxin to inhibit exocytosis (Amin et al., 2008). Notably, because mutations in *KDM5* genes cause modest changes in gene expression (Iwase et al., 2016; Scandaglia et al., 2017; Zamurrad et al., 2018), it is likely that the dysregulation of several genes in $kdm5^{JmjC*}$ mutant neurons contributes to the reduced synaptic transmission detected. Defining the precise role that these proteins play in mediating this synaptic phenotype will require further analyses of existing and additional ID-associated missense alleles that do, or do not, alter demethylase activity.

Our studies also emphasize the importance of other domains of KDM5, particularly the C5HC2 zinc-finger motif that is immediately adjacent to the JmjC domain and is affected by the L854F mutation. This motif has been suggested to be structurally required for JmjC domain function based on the crystal structure of KDM5A (Horton et al., 2016). It is also possible that the converse is true and that the JmjC domain contributes to C5HC2 function. Consistent with the JmjC and C5HC2 domains acting in concert with one another in some contexts, the $kdm5^{JmjC*}$ and $kdm5^{L854F}$ alleles showed a similar reduction in the number of NMJ synaptic boutons that contribute to muscle contraction and slowed larval movement. It is therefore possible that the bouton number and larval movement changes in $kdm5^{JmjC*}$ and $kdm5^{L854F}$ mutant larvae are functionally related, as similar correlations have been observed previously (Kashima et al., 2017). Moreover, a subset of the transcriptomic defects seen in these two genotypes was shared, suggesting a

possible molecular driver of the structural and functional phenotypes observed. Notably, this included diminished expression of *wingless* and ECM components that facilitate Wg signaling, which can result in reduced bouton number and slow larval locomotion (Kim and Cho, 2020). Alternatively, the bouton and movement phenotypes could have separate causes. The locomotor phenotype observed in $kdm5^{JmjC*}$ and $kdm5^{L854F}$ larvae may not be caused by NMJ perturbations but may instead be indirectly caused by aberrant neurotransmission in upstream motor networks or muscle deficits. Larval locomotion is a complex behavior that relies on linking appropriate sensory inputs with a wave of peristaltic muscle contractions that mediate larval movement (Kohsaka et al., 2017). As such, it is possible that the motor deficits displayed by $kdm5^{JmjC*}$ and $kdm5^{L854F}$ mutants are caused by synaptic or morphological changes in body-wall sensory neurons (Hughes and Thomas, 2007; Song et al., 2007) or defects in the premotor inhibitory interneurons (Kohsaka et al., 2014). Additional studies are needed to discern the functional links between KDM5-regulated transcription, changes in bouton number, and larval movement.

Our findings that $kdm5^{L854F}$ mutants possess larger boutons, which is not observed in $kdm5^{JmjC*}$, and displayed a number of unique gene expression defects suggest that the C5HC2 motif can also function independent of the JmjC domain. One key group of KDM5-regulated genes whose expression was disrupted by the L854F mutation were those involved in the regulation of the MT dynamics, which play key structural roles and transport roles in neurons (Conde and Cáceres, 2009). This observation may be important for the neuropathology of the equivalent mutation in human *KDM5C* (p.L731F) as changes to presynaptic MT physiology are observed in other ID disorders such fragile X syndrome (Bodaleo and Gonzalez-Billault, 2016; Lu et al., 2004). Moreover, restoring homeostasis to MT dynamics can attenuate morphological and functional phenotypes associated with mutations in the fragile X gene *fmr1* (Zhang et al., 2001). Further exploration of this potential link could highlight a means to attenuate the cognitive deficits for a subset of mutations associated with ID. Because no independent molecular function has been attributed to C5HC2 zinc-finger motifs, defining the precise molecular defect caused by changes to this domain in KDM5 family proteins will require additional analyses. In addition to being required for JmjC domain function, this motif might act as a protein-protein interaction motif and/or bind to nucleic acids (Riechmann et al., 2000; Secombe et al., 2007). Consequently, mutations in this region could therefore alter a range of functions that are critical for gene regulation, such as recruitment of KDM5 to its target genes and/or its ability to mediate activation or repression of transcription. Interestingly, the three mutations in the C5HC2 zinc finger examined do not result in the same NMJ phenotypes, suggesting that they may differentially affect KDM5 transcriptional regulation on synaptic target genes. Whereas $kdm5^{L854F}$ affected bouton number and size, $kdm5^{Y874C}$ appeared to modestly decrease bouton number and $kdm5^{R873W}$ NMJs were indistinguishable from WT. The more severe phenotypes of animals expressing the KDM5^{L854F} mutant protein are consistent with the amino acid substitution affecting one of the $Zn^{2+}$-binding sites in the C5CH2 domain. Indeed, DynaMut predictions suggested that this amino acid variation leads to significant alterations in the dynamics and stability around the C5HC2 motif, which could cause more dramatic changes both to transcription and to NMJ morphology.

In conclusion, we show that KDM5 is a key transcription regulator of genes important for synaptic structure and function. Our observations that KDM5 plays critical roles at the NMJ are consistent with accumulating data linking disruption of glutamatergic synapse to human cognitive disorders, including ID (Volk et al., 2015). Future studies will provide additional insights into how the individual domains of KDM5 contribute to its synaptic functions and how these activities are altered by ID-associated mutations.

## STAR★METHODS

Detailed methods are provided in the online version of this paper and include the following:

- KEY RESOURCES TABLE
- RESOURCE AVAILABILITY
  - Lead contact
  - Materials availability
  - Data and code availability
- EXPERIMENTAL MODEL AND SUBJECT DETAILS
  - Care of fly strains and crosses
  - Fly strains
- METHOD DETAILS
  - RNA-seq
  - Western blot
  - Immunostaining
  - Electrophysiology
  - Larval movement assays
  - Developmental timing quantification
  - Image acquisition and processing
  - *In silico* mutation analysis
- QUANTIFICATION AND STATISTICAL ANALYSIS
  - Statistical analyses

# Cell Reports
## Article

## REFERENCES

Amin, N.D., Zheng, Y.L., Kesavapany, S., Kanungo, J., Guszczynski, T., Sihag, R.K., Rudrabhatla, P., Albers, W., Grant, P., and Pant, H.C. (2008). Cyclin-dependent kinase 5 phosphorylation of human septin SEPT5 (hCDCrel-1) modulates exocytosis. J. Neurosci. 28, 3631–3643.

Ashburner, M., Ball, C.A., Blake, J.A., Botstein, D., Butler, H., Cherry, J.M., Davis, A.P., Dolinski, K., Dwight, S.S., Eppig, J.T., et al. (2000). Gene ontology: tool for the unification of biology. The Gene Ontology Consortium. Nat. Genet. 25, 25–29.

Banovic, D., Khorramshahi, O., Owald, D., Wichmann, C., Riedt, T., Fouquet, W., Tian, R., Sigrist, S.J., and Aberle, H. (2010). Drosophila neuroligin 1 promotes growth and postsynaptic differentiation at glutamatergic neuromuscular junctions. Neuron 66, 724–738.

Barski, A., Cuddapah, S., Cui, K., Roh, T.Y., Schones, D.E., Wang, Z., Wei, G., Chepelev, I., and Zhao, K. (2007). High-resolution profiling of histone methylations in the human genome. Cell 129, 823–837.

Bellosta, P., and Soldano, A. (2019). Dissecting the genetics of autism spectrum disorders: a Drosophila perspective. Front. Physiol. 10, 987.

Benayoun, B.A., Pollina, E.A., Ucar, D., Mahmoudi, S., Karra, K., Wong, E.D., Devarajan, K., Daugherty, A.C., Kundaje, A.B., Mancini, E., et al. (2014). H3K4me3 breadth is linked to cell identity and transcriptional consistency. Cell 158, 673–688.

Bischof, J., Maeda, R.K., Hediger, M., Karch, F., and Basler, K. (2007). An optimized transgenesis system for Drosophila using germ-line-specific phiC31 integrases. Proc. Natl. Acad. Sci. USA 104, 3312–3317.

Bodaleo, F.J., and Gonzalez-Billault, C. (2016). The presynaptic microtubule cytoskeleton in physiological and pathological conditions: lessons from Drosophila fragile X syndrome and hereditary spastic paraplegias. Front. Mol. Neurosci. 9, 60.

Brookes, E., Laurent, B., Õunap, K., Carroll, R., Moeschler, J.B., Field, M., Schwartz, C.E., Gecz, J., and Shi, Y. (2015). Mutations in the intellectual disability gene KDM5C reduce protein stability and demethylase activity. Hum. Mol. Genet. 24, 2861–2872.

Brunger, A.T., Choi, U.B., Lai, Y., Leitz, J., White, K.I., and Zhou, Q. (2019). The pre-synaptic fusion machinery. Curr. Opin. Struct. Biol. 54, 179–188.

Budnik, V., Koh, Y.H., Guan, B., Hartmann, B., Hough, C., Woods, D., and Gorczyca, M. (1996). Regulation of synapse structure and function by the Drosophila tumor suppressor gene dlg. Neuron 17, 627–640.

Chen, K., Luan, X., Liu, Q., Wang, J., Chang, X., Snijders, A.M., Mao, J.H., Secombe, J., Dan, Z., Chen, J.H., et al. (2019). Drosophila histone demethylase KDM5 regulates social behavior through immune control and gut microbiota maintenance. Cell Host Microbe 25, 537–552.e8.

Cheng, L., Locke, C., and Davis, G.W. (2011). S6 kinase localizes to the presynaptic active zone and functions with PDK1 to control synapse development. J. Cell Biol. 194, 921–935.

Coll-Tané, M., Krebbers, A., Castells-Nobau, A., Zweier, C., and Schenck, A. (2019). Intellectual disability and autism spectrum disorders 'on the fly': insights from Drosophila. Dis. Model. Mech. 12, dmm039180.

Conde, C., and Cáceres, A. (2009). Microtubule assembly, organization and dynamics in axons and dendrites. Nat. Rev. Neurosci. 10, 319–332.

De Rubeis, S., He, X., Goldberg, A.P., Poultney, C.S., Samocha, K., Cicek, A.E., Kou, Y., Liu, L., Fromer, M., Walker, S., et al.; DDD Study; Homozygosity Mapping Collaborative for Autism; UK10K Consortium (2014). Synaptic, transcriptional and chromatin genes disrupted in autism. Nature 515, 209–215.

DiAntonio, A. (2006). Glutamate receptors at the Drosophila neuromuscular junction. Int. Rev. Neurobiol. 75, 165–179.

Drelon, C., Belalcazar, H.M., and Secombe, J. (2018). The histone demethylase KDM5 is essential for larval growth in Drosophila. Genetics 209, 773–787.

Drelon, C., Rogers, M.F., Belalcazar, H.M., and Secombe, J. (2019). The histone demethylase KDM5 controls developmental timing in Drosophila by promoting prothoracic gland endocycles. Development 146, dev182568.

Feng, Y., Ueda, A., and Wu, C.F. (2004). A modified minimal hemolymph-like solution, HL3.1, for physiological recordings at the neuromuscular junctions of normal and mutant Drosophila larvae. J. Neurogenet. 18, 377–402.

Feuillette, S., Charbonnier, C., Frebourg, T., Campion, D., and Lecourtois, M. (2020). A connected network of interacting proteins is involved in human-Tau toxicity in Drosophila. Front. Neurosci. 14, 68.

Forrest, M.P., Parnell, E., and Penzes, P. (2018). Dendritic structural plasticity and neuropsychiatric disease. Nat. Rev. Neurosci. 19, 215–234.

Gonçalves, T.F., Gonçalves, A.P., Fintelman Rodrigues, N., dos Santos, J.M., Pimentel, M.M., and Santos-Rebouças, C.B. (2014). KDM5C mutational screening among males with intellectual disability suggestive of X-linked inheritance and review of the literature. Eur. J. Med. Genet. 57, 138–144.

Gramates, L.S., and Budnik, V. (1999). Assembly and maturation of the Drosophila larval neuromuscular junction. Int. Rev. Neurobiol. 43, 93–117.

Guruharsha, K.G., Rual, J.F., Zhai, B., Mintseris, J., Vaidya, P., Vaidya, N., Beekman, C., Wong, C., Rhee, D.Y., Cenaj, O., et al. (2011). A protein complex network of Drosophila melanogaster. Cell 147, 690–703.

Hakeda-Suzuki, S., Ng, J., Tzu, J., Dietzl, G., Sun, Y., Harms, M., Nardine, T., Luo, L., and Dickson, B.J. (2002). Rac function and regulation during Drosophila development. Nature 416, 438–442.

Horton, J.R., Engstrom, A., Zoeller, E.L., Liu, X., Shanks, J.R., Zhang, X., Johns, M.A., Vertino, P.M., Fu, H., and Cheng, X. (2016). Characterization of a linked Jumonji domain of the KDM5/JARID1 family of histone H3 lysine 4 demethylases. J. Biol. Chem. 291, 2631–2646.

Hughes, C.L., and Thomas, J.B. (2007). A sensory feedback circuit coordinates muscle activity in Drosophila. Mol. Cell. Neurosci. 35, 383–396.

Hyun, K., Jeon, J., Park, K., and Kim, J. (2017). Writing, erasing and reading histone lysine methylations. Exp. Mol. Med. 49, e324.

Iwase, S., Lan, F., Bayliss, P., de la Torre-Ubieta, L., Huarte, M., Qi, H.H., Whetstine, J.R., Bonni, A., Roberts, T.M., and Shi, Y. (2007). The X-linked mental retardation gene SMCX/JARID1C defines a family of histone H3 lysine 4 demethylases. Cell 128, 1077–1088.

Iwase, S., Brookes, E., Agarwal, S., Badeaux, A.I., Ito, H., Vallianatos, C.N., Tomassy, G.S., Kasza, T., Lin, G., Thompson, A., et al. (2016). A mouse model of X-linked intellectual disability associated with impaired removal of histone methylation. Cell Rep. 14, 1000–1009.

Iwase, S., Bérubé, N.G., Zhou, Z., Kasri, N.N., Battaglioli, E., Scandaglia, M., and Barco, A. (2017). Epigenetic etiology of intellectual disability. J. Neurosci. 37, 10773–10782.

Jensen, L.R., Amende, M., Gurok, U., Moser, B., Gimmel, V., Tzschach, A., Janecke, A.R., Tariverdian, G., Chelly, J., Fryns, J.P., et al. (2005). Mutations in the JARID1C gene, which is involved in transcriptional regulation and chromatin remodeling, cause X-linked mental retardation. Am. J. Hum. Genet. 76, 227–236.

Kashima, R., Redmond, P.L., Ghatpande, P., Roy, S., Kornberg, T.B., Hanke, T., Knapp, S., Lagna, G., and Hata, A. (2017). Hyperactive locomotion in a

*Drosophila* model is a functional readout for the synaptic abnormalities underlying fragile X syndrome. Sci. Signal. *10*, eaai8133.

Kim, Y., and Cho, K.O. (2020). POU domain motif3 (Pdm3) induces wingless (wg) transcription and is essential for development of larval neuromuscular junctions in *Drosophila*. Sci. Rep. *10*, 517.

Kim, J.H., Lee, J.H., Lee, I.S., Lee, S.B., and Cho, K.S. (2017). Histone lysine methylation and neurodevelopmental disorders. Int. J. Mol. Sci. *18*, 1404.

Koh, Y.H., Gramates, L.S., and Budnik, V. (2000). *Drosophila* larval neuromuscular junction: molecular components and mechanisms underlying synaptic plasticity. Microsc. Res. Tech. *49*, 14–25.

Kohsaka, H., Takasu, E., Morimoto, T., and Nose, A. (2014). A group of segmental premotor interneurons regulates the speed of axial locomotion in *Drosophila* larvae. Curr. Biol. *24*, 2632–2642.

Kohsaka, H., Guertin, P.A., and Nose, A. (2017). Neural circuits underlying fly larval locomotion. Curr. Pharm. Des. *23*, 1722–1733.

Langmead, B., and Salzberg, S.L. (2012). Fast gapped-read alignment with Bowtie 2. Nat. Methods *9*, 357–359.

Lebrun, N., Mehler-Jacob, C., Poirier, K., Zordan, C., Lacombe, D., Carion, N., Billuart, P., and Bienvenu, T. (2018). Novel KDM5B splice variants identified in patients with developmental disorders: functional consequences. Gene *679*, 305–313.

Li, J., Ashley, J., Budnik, V., and Bhat, M.A. (2007). Crucial role of *Drosophila* neurexin in proper active zone apposition to postsynaptic densities, synaptic growth, and synaptic transmission. Neuron *55*, 741–755.

Li, L., Greer, C., Eisenman, R.N., and Secombe, J. (2010). Essential functions of the histone demethylase Lid. PLoS Genet. *6*, e1001221.

Liu, X., and Secombe, J. (2015). The histone demethylase KDM5 activates gene expression by recognizing chromatin context through its PHD reader motif. Cell Rep. *13*, 2219–2231.

Liu, X., Greer, C., and Secombe, J. (2014). KDM5 interacts with Foxo to modulate cellular levels of oxidative stress. PLoS Genet. *10*, e1004676.

Long, A.A., Mahapatra, C.T., Woodruff, E.A., III, Rohrbough, J., Leung, H.T., Shino, S., An, L., Doerge, R.W., Metzstein, M.M., Pak, W.L., and Broadie, K. (2010). The nonsense-mediated decay pathway maintains synapse architecture and synaptic vesicle cycle efficacy. J. Cell Sci. *123*, 3303–3315.

Love, M.I., Huber, W., and Anders, S. (2014). Moderated estimation of fold change and dispersion for RNA-seq data with DESeq2. Genome Biol. *15*, 550.

Lu, R., Wang, H., Liang, Z., Ku, L., O'Donnell, W.T., Li, W., Warren, S.T., and Feng, Y. (2004). The fragile X protein controls microtubule-associated protein 1B translation and microtubule stability in brain neuron development. Proc. Natl. Acad. Sci. USA *101*, 15201–15206.

Mariani, L., Lussi, Y.C., Vandamme, J., Riveiro, A., and Salcini, A.E. (2016). The H3K4me3/2 histone demethylase RBR-2 controls axon guidance by repressing the actin-remodeling gene wsp-1. Development *143*, 851–863.

Marttinen, M., Kurkinen, K.M., Soininen, H., Haapasalo, A., and Hiltunen, M. (2015). Synaptic dysfunction and septin protein family members in neurodegenerative diseases. Mol. Neurodegener. *10*, 16.

Menon, K.P., Carrillo, R.A., and Zinn, K. (2013). Development and plasticity of the *Drosophila* larval neuromuscular junction. Wiley Interdiscip. Rev. Dev. Biol. *2*, 647–670.

Mi, H., Dong, Q., Muruganujan, A., Gaudet, P., Lewis, S., and Thomas, P.D. (2010). PANTHER version 7: improved phylogenetic trees, orthologs and collaboration with the Gene Ontology Consortium. Nucleic Acids Res. *38*, D204–D210.

Moretto, E., Murru, L., Martano, G., Sassone, J., and Passafaro, M. (2018). Glutamatergic synapses in neurodevelopmental disorders. Prog. Neuropsychopharmacol. Biol. Psychiatry *84*, 328–342.

Nägerl, U.V., Eberhorn, N., Cambridge, S.B., and Bonhoeffer, T. (2004). Bidirectional activity-dependent morphological plasticity in hippocampal neurons. Neuron *44*, 759–767.

Najmabadi, H., Hu, H., Garshasbi, M., Zemojtel, T., Abedini, S.S., Chen, W., Hosseini, M., Behjati, F., Haas, S., Jamali, P., et al. (2011). Deep sequencing reveals 50 novel genes for recessive cognitive disorders. Nature *478*, 57–63.

Navarro-Costa, P., McCarthy, A., Prudêncio, P., Greer, C., Guilgur, L.G., Becker, J.D., Secombe, J., Rangan, P., and Martinho, R.G. (2016). Early programming of the oocyte epigenome temporally controls late prophase I transcription and chromatin remodelling. Nat. Commun. *7*, 12331.

Nechipurenko, I.V., and Broihier, H.T. (2012). FoxO limits microtubule stability and is itself negatively regulated by microtubule disruption. J. Cell Biol. *196*, 345–362.

Neufeld, T.P., de la Cruz, A.F., Johnston, L.A., and Edgar, B.A. (1998). Coordination of growth and cell division in the *Drosophila* wing. Cell *93*, 1183–1193.

Newman, Z.L., Hoagland, A., Aghi, K., Worden, K., Levy, S.L., Son, J.H., Lee, L.P., and Isacoff, E.Y. (2017). Input-specific plasticity and homeostasis at the *Drosophila* larval neuromuscular junction. Neuron *93*, 1388–1404.e10.

Packard, M., Koo, E.S., Gorczyca, M., Sharpe, J., Cumberledge, S., and Budnik, V. (2002). The *Drosophila* Wnt, wingless, provides an essential signal for pre- and postsynaptic differentiation. Cell *111*, 319–330.

Pettersen, E.F., Goddard, T.D., Huang, C.C., Couch, G.S., Greenblatt, D.M., Meng, E.C., and Ferrin, T.E. (2004). UCSF Chimera—a visualization system for exploratory research and analysis. J. Comput. Chem. *25*, 1605–1612.

Rasse, T.M., Fouquet, W., Schmid, A., Kittel, R.J., Mertel, S., Sigrist, C.B., Schmidt, M., Guzman, A., Merino, C., Qin, G., et al. (2005). Glutamate receptor dynamics organizing synapse formation *in vivo*. Nat. Neurosci. *8*, 898–905.

Riechmann, J.L., Heard, J., Martin, G., Reuber, L., Jiang, C., Keddie, J., Adam, L., Pineda, O., Ratcliffe, O.J., Samaha, R.R., et al. (2000). *Arabidopsis* transcription factors: genome-wide comparative analysis among eukaryotes. Science *290*, 2105–2110.

Rodrigues, C.H., Pires, D.E., and Ascher, D.B. (2018). DynaMut: predicting the impact of mutations on protein conformation, flexibility and stability. Nucleic Acids Res. *46*, W350–W355.

Ronan, J.L., Wu, W., and Crabtree, G.R. (2013). From neural development to cognition: unexpected roles for chromatin. Nat. Rev. Genet. *14*, 347–359.

Roos, J., Hummel, T., Ng, N., Klämbt, C., and Davis, G.W. (2000). *Drosophila* Futsch regulates synaptic microtubule organization and is necessary for synaptic growth. Neuron *26*, 371–382.

Rujirabanjerd, S., Nelson, J., Tarpey, P.S., Hackett, A., Edkins, S., Raymond, F.L., Schwartz, C.E., Turner, G., Iwase, S., Shi, Y., et al. (2010). Identification and characterization of two novel JARID1C mutations: suggestion of an emerging genotype-phenotype correlation. Eur. J. Hum. Genet. *18*, 330–335.

Scandaglia, M., Lopez-Atalaya, J.P., Medrano-Fernandez, A., Lopez-Cascales, M.T., Del Blanco, B., Lipinski, M., Benito, E., Olivares, R., Iwase, S., Shi, Y., and Barco, A. (2017). Loss of Kdm5c causes spurious transcription and prevents the fine-tuning of activity-regulated enhancers in neurons. Cell Rep. *21*, 47–59.

Secombe, J., Li, L., Carlos, L., and Eisenman, R.N. (2007). The Trithorax group protein Lid is a trimethyl histone H3K4 demethylase required for dMyc-induced cell growth. Genes Dev. *21*, 537–551.

Shannon, P., Markiel, A., Ozier, O., Baliga, N.S., Wang, J.T., Ramage, D., Amin, N., Schwikowski, B., and Ideker, T. (2003). Cytoscape: a software environment for integrated models of biomolecular interaction networks. Genome Res. *13*, 2498–2504.

Soneson, C., and Delorenzi, M. (2013). A comparison of methods for differential expression analysis of RNA-seq data. BMC Bioinformatics *14*, 91.

Song, W., Onishi, M., Jan, L.Y., and Jan, Y.N. (2007). Peripheral multidendritic sensory neurons are necessary for rhythmic locomotion behavior in *Drosophila* larvae. Proc. Natl. Acad. Sci. USA *104*, 5199–5204.

Stenson, P.D., Mort, M., Ball, E.V., Evans, K., Hayden, M., Heywood, S., Hussain, M., Phillips, A.D., and Cooper, D.N. (2017). The Human Gene Mutation Database: towards a comprehensive repository of inherited mutation data for medical research, genetic diagnosis and next-generation sequencing studies. Hum. Genet. *136*, 665–677.

Szklarczyk, D., Gable, A.L., Lyon, D., Junge, A., Wyder, S., Huerta-Cepas, J., Simonovic, M., Doncheva, N.T., Morris, J.H., Bork, P., et al. (2019). STRING v11: protein-protein association networks with increased coverage, supporting functional discovery in genome-wide experimental datasets. Nucleic Acids Res. *47*, D607–D613.

Tahiliani, M., Mei, P., Fang, R., Leonor, T., Rutenberg, M., Shimizu, F., Li, J., Rao, A., and Shi, Y. (2007). The histone H3K4 demethylase SMCX links REST target genes to X-linked mental retardation. Nature *447*, 601–605.

Trogden, K.P., and Rogers, S.L. (2015). TOG proteins are spatially regulated by Rac-GSK3β to control interphase microtubule dynamics. PLoS One *10*, e0138966.

Tzschach, A., Lenzner, S., Moser, B., Reinhardt, R., Chelly, J., Fryns, J.P., Kleefstra, T., Raynaud, M., Turner, G., Ropers, H.H., et al. (2006). Novel JAR-ID1C/SMCX mutations in patients with X-linked mental retardation. Hum. Mutat. *27*, 389.

Vallianatos, C.N., and Iwase, S. (2015). Disrupted intricacy of histone H3K4 methylation in neurodevelopmental disorders. Epigenomics *7*, 503–519.

Vallianatos, C.N., Farrehi, C., Friez, M.J., Burmeister, M., Keegan, C.E., and Iwase, S. (2018). Altered gene-regulatory function of KDM5C by a novel mutation associated with autism and intellectual disability. Front. Mol. Neurosci. *11*, 104.

Vallianatos, C.N., Raines, B., Porter, R.S., Bonefas, K.M., Wu, M.C., Garay, P.M., Collette, K.M., Seo, Y.A., Dou, Y., Keegan, C.E., et al. (2020). Mutually suppressive roles of KMT2A and KDM5C in behaviour, neuronal structure, and histone H3K4 methylation. Commun. Biol. *3*, 278.

Vasin, A., Zueva, L., Torrez, C., Volfson, D., Littleton, J.T., and Bykhovskaia, M. (2014). Synapsin regulates activity-dependent outgrowth of synaptic boutons at the *Drosophila* neuromuscular junction. J. Neurosci. *34*, 10554–10563.

Verpelli, C., Piccoli, G., Zibetti, C., Zanchi, A., Gardoni, F., Huang, K., Brambilla, D., Di Luca, M., Battaglioli, E., and Sala, C. (2010). Synaptic activity controls dendritic spine morphology by modulating eEF2-dependent BDNF synthesis. J. Neurosci. *30*, 5830–5842.

Vinogradova, M., Gehling, V.S., Gustafson, A., Arora, S., Tindell, C.A., Wilson, C., Williamson, K.E., Guler, G.D., Gangurde, P., Manieri, W., et al. (2016). An inhibitor of KDM5 demethylases reduces survival of drug-tolerant cancer cells. Nat. Chem. Biol. *12*, 531–538.

Viquez, N.M., Li, C.R., Wairkar, Y.P., and DiAntonio, A. (2006). The B′ protein phosphatase 2A regulatory subunit well-rounded regulates synaptic growth and cytoskeletal stability at the *Drosophila* neuromuscular junction. J. Neurosci. *26*, 9293–9303.

Volk, L., Chiu, S.L., Sharma, K., and Huganir, R.L. (2015). Glutamate synapses in human cognitive disorders. Annu. Rev. Neurosci. *38*, 127–149.

Wagner, N., Laugks, U., Heckmann, M., Asan, E., and Neuser, K. (2015). Aging *Drosophila melanogaster* display altered pre- and postsynaptic ultrastructure at adult neuromuscular junctions. J. Comp. Neurol. *523*, 2457–2475.

Xing, G., Li, M., Sun, Y., Rui, M., Zhuang, Y., Lv, H., Han, J., Jia, Z., and Xie, W. (2018). Neurexin-neuroligin 1 regulates synaptic morphology and functions via the WAVE regulatory complex in *Drosophila* neuromuscular junction. eLife *7*, e30457.

Yang, Y.M., Fedchyshyn, M.J., Grande, G., Aitoubah, J., Tsang, C.W., Xie, H., Ackerley, C.A., Trimble, W.S., and Wang, L.Y. (2010). Septins regulate developmental switching from microdomain to nanodomain coupling of Ca(2+) influx to neurotransmitter release at a central synapse. Neuron *67*, 100–115.

Zamurrad, S., Hatch, H.A.M., Drelon, C., Belalcazar, H.M., and Secombe, J. (2018). A *Drosophila* model of intellectual disability caused by mutations in the histone demethylase KDM5. Cell Rep. *22*, 2359–2369.

Zhang, Y.Q., Bailey, A.M., Matthies, H.J., Renden, R.B., Smith, M.A., Speese, S.D., Rubin, G.M., and Broadie, K. (2001). *Drosophila* fragile X-related gene regulates the MAP1B homolog Futsch to control synaptic structure and function. Cell *107*, 591–603.

# STAR★METHODS

## KEY RESOURCES TABLE

| REAGENT or RESOURCE | SOURCE | IDENTIFIER |
| --- | --- | --- |
| **Antibodies** | | |
| Mouse monoclonal anti-histone H3 | Abcam | Cat#24834; RRID: AB_470335 |
| Rabbit polyclonal anti-H3K4me3 | Active motif | Cat#39159; RRID: AB_2615077 |
| Mouse monoclonal anti-HA | Cell signaling | Cat#2367S; RRID: AB_10691311 |
| Rabbit polyclonal anti-KDM5 | Secombe et al., 2007 | N/A |
| Anti-gamma-tubulin (Clone 4D11) | Invitrogen | Cat#MA1-850; RRID: AB_2211249 |
| Mouse monoclonal anti alpha-Tubulin | Developmental Studies Hybridoma Bank, University of Iowa | Cat#12G10; RRID: AB_1157911 |
| Mouse monoclonal anti Dlg | Developmental Studies Hybridoma Bank, University of Iowa | Cat#4F3; RRID: AB_528203 |
| Mouse monoclonal anti-Futsch | Developmental Studies Hybridoma Bank, University of Iowa | Cat#22C10; RRID: AB_528403 |
| Mouse monoclonal anti Brp | Developmental Studies Hybridoma Bank, University of Iowa | Cat#nc82; RRID: AB_2314866 |
| Alexa 647-conjugated goat anti-HRP | Jackson ImmunoResearch Laboratories | Cat# 123-605-021; RRID: AB_2338967 |
| Rabbit polyclonal anti- GluRIIC | Aaron DiAntonio | N/A |
| IRDye® 800CW Donkey anti-Rabbit IgG | LI-COR | Cat#92632213; RRID: AB_621848 |
| IRDye® 680RD Donkey anti-Mouse IgG | LI-COR | Cat#925-68072; RRID: AB_10953628 |
| Goat anti-Mouse IgG (H+L) Alexa Fluor Plus 488 | ThermoFisher | Catalog# A32723 |
| Goat anti-mouse TRITC | Jackson ImmunoResearch Laboratories | 111-025-003 RRID:AB_2337926 |
| Goat anti-rabbit FITC | Jackson ImmunoResearch Laboratories | 111-095-003 RRID:AB_2337972 |
| **Chemicals, peptides, and recombinant proteins** | | |
| SlowFade Glass Antifade Mountant | Invitrogen | Cat#S36918 |
| Fluoromount-G DAPI | SouthernBiotech | Cat#0100.01 |
| Trehalose | Sigma | Cat# PHR1344 |
| TRIZOL RNA Isolation Reagent | Invitrogen | Cat#15596026 |
| **Critical commercial assays** | | |
| In-Fusion® HD Cloning Plus | Takara | Cat# 638909 |
| TruSeq Stranded mRNA Library | Illumina | Cat#20020594 |
| **Deposited data** | | |
| Third instar VNC-$kdm5^{WT}$ RNA-seq | This paper | GEO: GSE159298 |
| Third instar VNC-$kdm5^{JmjC*}$ RNA-seq | This paper | GEO: GSE159298 |
| Third instar VNC-$kdm5^{L854F}$ RNA-seq | This paper | GEO: GSE159298 |
| **Experimental models: organisms/strains** | | |
| *UASp-kdm5* | Secombe et al., 2007 | N/A |
| *UAS-shRNA-kdm5* | Bloomington Drosophila Stock Center (BDSC) | BL35706 |
| *kdm5$^{140}$/Cyo-GFP* | Drelon et. al, 2018 | N/A |
| *kdm5$^{140}$/Cyo-GFP; UASp-kdm5* | Drelon et. al, 2019 | N/A |
| *kdm5$^{140}$,OK6-Gal4/Cyo-GFP* | This study | N/A |
| *kdm5$^{140}$/Cyo-GFP;repo-Gal4/TM6B* | This study | N/A |
| *kdm5$^{140}$/Cyo-GFP;Mef2-Gal4* | This study | N/A |
| *elav-Gal4; kdm5$^{140}$/Cyo-GFP* | This study | N/A |
| *kdm5$^{140}$/Cyo-GFP;actin-Gal4/TM6B* | This study | N/A |

*Continued*

| REAGENT or RESOURCE | SOURCE | IDENTIFIER |
|---|---|---|
| *kdm5$^{140}$/Cyo-GFP;da-Gal4/TM6B* | This study | N/A |
| *Kdm5$^{140}$; kdm5$^{WT}$* in attP86F | Navarro-Costa et al., 2016 | N/A |
| *kdm5$^{140}$;kdm5$^{JmjC*}$* in attP86F | Navarro-Costa et. al, 2016 | N/A |
| *kdm5$^{140}$;kdm5$^{L854F}$* in attP86F | This study | N/A |
| *kdm5$^{140}$;kdm5$^{R873W}$* in attP86F | This study | N/A |
| *kdm5$^{140}$;kdm5$^{Y874C}$* in attP86F | This study | N/A |
| *w$^{1118}$* | BDSC | BL5905 |
| FlyC31 | BDSC | BL24749 |
| *OK6-Gal4* | BDSC | BL64199 |
| *Elav-Gal4* | BDSC | BL25750 |
| *Act5C-Gal4* | BDSC | BL3954 |
| *da-Gal4* | BDSC | BL55851 |
| *Mef2-Gal4* | BDSC | BL27390 |
| *repo-Gal4* | BDSC | BL7415 |
| Recombinant DNA | | |
| pattB | Drosophila Genomics Resource Center | Cat 1420 |
| Software and algorithms | | |
| LI-COR Image Studio | https://www.licor.com | RRID:SCR_015795 |
| Adobe Illustrator CC 2021 | https://www.adobe.com/ | RRID: SCR_010279 |
| AxioVision Release 4.8 | Zeiss | RRID:SCR_002677 |
| UCSF Chimera | UCSF Resource for Biocomputing, Visualization, and Informatics | RRID:SCR_004097 |
| Pymol | http://www.pymol.org/ | RRID:SCR_000305 |
| GraphPad Prism 8 | GraphPad Software, Inc. | RRID: SCR_002798 |
| FIJI (ImageJ) | National Institutes of Health | RRID:SCR_003070 |
| pClamp | v11.0, Molecular Devices | RRID:SCR_011323 |
| Bowtie2 (v2.2.5) | Langmead and Salzberg, 2012 | RRID:SCR_005476 |
| R package DESeq2 | Love et al., 2014 | RRID:SCR_015687 |
| Other | | |
| DynaMut server | Rodrigues et al., 2018 | N/A |
| Biorender | http://biorender.com | RRID:SCR_018361 |
| String | http://string.embl.de/ | RRID:SCR_005223 |
| GeneOntology | (Ashburner et al., 2000) | N/A |

## RESOURCE AVAILABILITY

### Lead contact
Further information and requests for resources and reagents should be directed to the Lead Contact, Julie Secombe (Julie.Secombe@einsteinmed.org).

### Materials availability
All fly strains described in this manuscript are available upon request.

### Data and code availability
The accession number for the RNA-seq data reported in this paper is NCBI Gene Expression Omnibus GEO:GSE159298. A list of differentially expressed genes (and log2 fold change) observed compared to wild-type are provided in Tables S1 and S2 (5% FDR) for *kdm5$^{JmjC*}$* and *kdm5$^{L854F}$*, respectively.

## EXPERIMENTAL MODEL AND SUBJECT DETAILS

### Care of fly strains and crosses

Fly crosses were maintained at 25°C with 50% humidity and a 12-hour light/dark cycle. Food (per liter) contained 18 g yeast, 22 g molasses, 80 g malt extract, 9g agar, 65 cornmeal, 2.3g methyl para-benzoic acid, 6.35ml propionic acid. The number of male and female larvae were equal across the genotypes examined. For studies comparing wild-type and *kdm5* mutant larvae, animals were matched for developmental stage based on the morphology of larval mouth hooks, not chronological age, similar to our previously reported analyses (Drelon et al., 2018, 2019). Control wandering third instar larvae were therefore ~120 hours after egg laying (AEL) while *kdm5*[140] larvae were 8-10 days old.

### Fly strains

The *kdm5*[140] null and *kdm5*[JmjC*] alleles have been previously described (Drelon et al., 2018; Navarro-Costa et al., 2016; Zamurrad et al., 2018). *UASp-kdm5* transgene was validated in numerous rescue experiments (Drelon et al., 2019; Li et al., 2010; Secombe et al., 2007). The *UAS-shRNA* transgene to knockdown *kdm5* was generated as part of the TRiP project and has been well-validated by us and others (BL #35706) (Liu et al., 2014; Navarro-Costa et al., 2016). To generate ID alleles, we took a similar approach as our previous analyses of *kdm5*[JmjC*] (Drelon et al., 2018, 2019; Navarro-Costa et al., 2016). Briefly, the 11kb genomic region encompassing *kdm5* was amplified by PCR from *w*[1118] and cloned into the pattB vector (Bischof et al., 2007) using the In-Fusion cloning system (Takara). A 3xHA tag was included in-frame at the 3'end of the *kdm5* ORF. Point mutations (L854F, R873W, Y874C) were introduced by PCR-mediated site-directed mutagenesis. Sequenced constructs were sent to BestGene for injection into FlyC31 embryos (BL #24749). Transformed flies were crossed into the *kdm5*[140] null background and homozygous stocks were established. Wild-type and demethylase dead transgenes and resulting fly strains are published (Navarro-Costa et al., 2016; Zamurrad et al., 2018). Gal4 driver fly strains used included *OK6-Gal4* (BL #64199), *elav-Gal4* (BL#25750), *Act5C-Gal4* (BL #3954), *da-Gal4* (BL #55851), *Mef2-Gal4* (BL #27390), *repo-Gal4* (BL #7415). Gal4 expression was validated by crossing each Gal4 strain with the UAS.GFPnls reporter line (Neufeld et al., 1998).

## METHOD DETAILS

### RNA-seq

Pooled male and female CNSs from wild-type (*kdm5*[WT]), *kdm5*[JmjC*], and *kdm5*[L854F] third instar larvae were dissected Hemolymph-Like Solution (HL-3: NaCl 70mM, KCl 5mM, MgCl$_2$ 20mM, NaHCO$_3$ 10mM, trehalose 5mM, sucrose 115mM, HEPES 5mM, pH7.1) without CaCl$^2$ and brain lobes were separated to enrich for VNC cells. Total RNA was isolated with Trizol (Invitrogen) and quality was assessed by Fragment Analyzer (Advanced Analytical, Ankeny, IA, USA) before sending to the Beijing Genomics Institute (BGI) for library preparation and sequencing. cDNA libraries were prepared using TruSeq Stranded mRNA Library. mRNAs were isolated from total RNA with oligo(dT) method. After mRNA fragmentation, first strand cDNA and second strand cDNA were synthesized, and cDNA fragments were purified and resolved with EB buffer for end reparation and single nucleotide A (adenine) addition. cDNA fragments were linked with adapters and those with suitable sizes were selected for PCR amplification. Libraries were sequenced on Illumina NovaSeq 6000 platform. Alignment of raw reads to the reference genome (dm6) was performed using Bowtie2 (v2.2.5) (Langmead and Salzberg, 2012), normalized and differential expression determined with DESeq2 package (Love et al., 2014; Soneson and Delorenzi, 2013).

   Gene Ontology (GO) enrichment analysis of protein-coding genes found to be dysregulated in *kdm5*[JmjC*] and/or *kdm5*[L854F] RNA-seq data (5% FDR cutoff) was carried out using PANTHER overrepresentation test (http://geneontology.org/) (Mi et al., 2010) and String (http://string-db.org) v11.0b (Szklarczyk et al., 2019). Interaction networks were determined using String (Szklarczyk et al., 2019) and visualized using Cytoscape (Shannon et al., 2003).

### Western blot

Third instar larval brains were dissected in ice-cold 1xPBS. Samples were stored in 2x NuPAGE LDS Buffer at −20°C until use. After a round of sonication and treatment with DTT, samples were subjected to SDS-PAGE and transferred to a PVDF membrane for immunoblotting. Membranes were incubated with primary antibodies at 4°C overnight, washed and incubated with secondary antibodies at room temperature for 30min. Mouse anti-histone H3, 1:2000 (Abcam #24834); rabbit anti-H3K4me3 1:2000 (Active Motif #39159); mouse anti-HA, 1:500 (Cell Signaling #2367S); rabbit anti-KDM5, 1:250 (Secombe et al., 2007); anti-gamma-tubulin, 1:1000 (4D11; Invitrogen MA1-850); and mouse anti alpha-Tubulin, 1:10000 (12G10, Developmental Studies Hybridoma Bank, University of Iowa) were used as primary antibodies. IRDye® 800CW Donkey anti-Rabbit IgG (92632213) and IRDye® 680RD Donkey anti-Mouse IgG (925-68072) from LI-COR were used as secondary antibodies. Western blots were quantified using LI-COR Image Studio software.

### Immunostaining

Third instar larvae were dissected in ice-cold 1xPBS and fillets were fixed in 4%PFA in PBS at room temperature for 30min. For Futsch staining, fillets were fixed in ice-cold methanol for 10min at −20°C. Samples were washed in 1xPBS for 10 min followed by two washes in 1xPBST (PBS + 0.1% Triton) for 10min each. Fillets were transferred to 0.5μl tubes for primary antibody incubation overnight at 4°C with agitation. After three 15 min washes in 1xPBST, samples were incubated in secondary antibodies for 1 h at room

temperature. Samples were then washed three times for 10 min each and mounted with Fluoromount-G DAPI (SouthernBiotech) or SlowFade Glass Antifade Mountant (Invitrogen). Mouse anti-Dlg (4F3) 1:1000, anti-Futsch (22C10) 1:100, and anti Brp (nc82) 1:100 were obtained from Developmental Studies Hybridoma Bank (DSHB, University of Iowa). Rabbit anti- GluRIIC (1:5000) was a kind gift from Aaron DiAntonio. Alexa 647-conjugated goat anti-HRP was used at 1:200 (Jackson ImmunoResearch Laboratories, Inc., West Grove, PA). Goat anti-mouse Alexa 488 (Invitrogen) was used at 1:400 while goat anti-mouse TRITC and anti-rabbit FITC (Jackson ImmunoResearch Laboratories, Inc., West Grove, PA) were used at 1:400.

## Electrophysiology

Third instar larvae were fillet dissected in ice cold HL-3.1 (Feng et al., 2004) containing 0.25 mM $Ca^{2+}$. Larvae were glued (Vetbond Tissue Adhesive, World Precision Instruments) to Sylgard-coated coverslips, the VNC was cut out of the animal, and the HL-3.1 was replaced with room temperature HL-3.1 containing 1.0 mM $Ca^{2+}$ for recordings. Muscle 6 in segments A3 or A4 was voltage clamped at −60 mV using an Axoclamp 900A amplier (Molecular Devices). Clamp and recording electrodes with 10-20 MΩ of resistance were filled with 3 mM KCl. Supra threshold stimuli were delivered via stimulating electrodes filled with bath solution using a Grass S88 stimulator with a SIU5 isolation unit (Grass Technologies). Evoked EJCs were measured after stimulating segmental nerves at 0.2 Hz for 50 s to establish baseline responses. Endocytosis was assessed by stimulating by 20 Hz for 60 s. Recovery of the cycling pool of vesicles was assessed by stimulating at 0.2 Hz for 50 s. Paired pulse amplitudes were measured after delivering two 10 Hz, two 20 Hz, two 50 Hz, and two 100 Hz pulses, each of which were separated by a 20 s intertrial interval. Recordings were digitized with a Digidata 1443 digitizer (Molecular Devices). Quantal content was calculated by dividing the eEJC area (nA × ms) by the mEJC area (nA × ms) for each animal. 180 s of spontaneous activity was used to quantify mEJC frequency and amplitude. An equal number of recordings from controls and experimental animals were obtained each day. Data were analyzed in pClamp (v11.0, Molecular Devices).

## Larval movement assays

Third instar larvae were placed on Petri dishes containing 1.6% agar in double distilled water. Larvae were allowed to crawl on the agar dish for one minute to remove excess food and then transferred to the crawling arena, which also consisted of 1.6% agar. Larvae were allowed to acclimate for one minute then larval locomotion was recorded using a Cannon EOS M50 camera at 29.97 frames per second for 30 s. Five larvae were recorded per video. Videos were opened in ImageJ (NIH) and 899 frames were analyzed with the publicly available wrMTrck plugin (Jesper S. Pedersen; https://www.phage.dk/plugins/wrmtrck.html).

## Developmental timing quantification

Female and male flies were placed in a vial and allowed to lay eggs for 24 hours. Starting at day 5 after egg laying the number of animals that had pupariated were scored twice per day.

## Image acquisition and processing

Images of NMJs from muscles 4 and 6 of abdominal segment 3 were acquired using Leica Sp8 Confocal Microscope, 63x/1.4NA and Zeiss Axioimager Z1 Apotome. Quantification of muscle area and type Ib bouton number and area were performed in the Dlg channel using ImageJ. The number of boutons was normalized to muscle surface area similar to previous studies (Banovic et al., 2010; Nechipurenko and Broihier, 2012). The Threshold and Measure commands were used to quantify bouton surface areas, similar to previous studies (Wagner et al., 2015). Adult fly images were obtained using a stereomicroscope Carl Zeiss Stereo Discovery V12 with 14X magnification and captured using AxioVision Release 4.8 software. Brp density was calculated by dividing the total Brp puncta by the NMJ area. Colocalization of Brp and GluRIIC was quantified using Fiji (NIH ImageJ) by outlining the NMJ in a max-projected image. Pearson's R values were obtained for each image after splitting the channels using the Coloc2 plugin. All images were processed and assembled into figure format using Adobe Illustrator 2021. Images of adult head and ventral nerve cord and icons used in the model were created with BioRender.com.

## *In silico* mutation analysis

Normal mode analysis was used to predict the thermodynamic changes upon mutations in the human KDM5A structure (PDB: 5CEH) via the DynaMut server (Rodrigues et al., 2018). Files generated by DynaMut were visualized using PyMol (The PyMOL Molecular Graphics System, Version 2.4 Schrödinger, LLC). UCSF's Chimera (Pettersen et al., 2004) was used to modify the KDM5A structure.

## QUANTIFICATION AND STATISTICAL ANALYSIS

## Statistical analyses

All experiments were performed in biological triplicate (minimum) and numbers (n) are provided for each experiment either in the figure or the legend. Student's t tests were used for pairwise comparisons while one-way ANOVAs were used for three or more groups, followed by Dunn's or Dunnett's multiple comparisons tests. Fisher's exact test was used to analyze contingency tables (Survival adult flies and overlapping genes). To test the directionality of expression changes in overlapping genes, Spearman correlation was used. Two-way ANOVAs were used to analyze high frequency stimulation. GraphPad Prism (v8.4) or R version 3.6.2 was used for analyses. Error bars on graphs represent mean ±SEM.
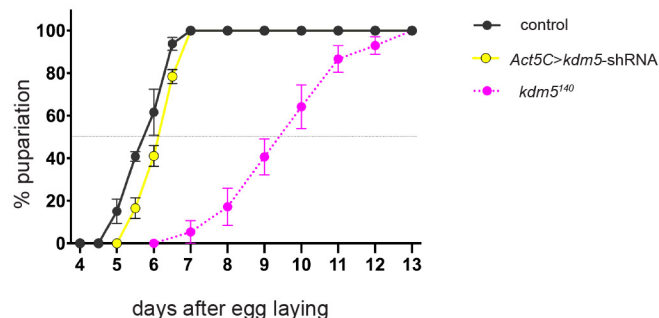
# Supplemental Information

# The histone demethylase KDM5 is required

# for synaptic structure and function

# at the *Drosophila* neuromuscular junction

Helen M. Belalcazar, Emily L. Hendricks, Sumaira Zamurrad, Faith L.W. Liebl, and Julie Secombe

**A** kdm5 knockdown developmental timing

- control
- Act5C>kdm5-shRNA
- kdm5[140]

% pupariation vs days after egg laying

**B**

control / Act5C>kdm5-shRNA
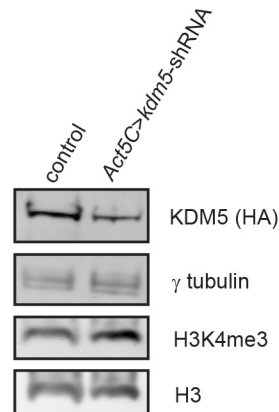
KDM5 (HA)

γ tubulin

H3K4me3

H3

**Figure S1. Ubiquitous *kdm5* knockdown affects levels of H3K4me3 without grossly affecting developmental timing. Related to Figure 1.**

(A) Developmental timing of control (*w[1118]*), *kdm5[140]*, and the *kdm5* knockdown *Act5C>kdm5*-shRNA determining the day when 50% of the animals reach pupariation. Total pupae quantified in three different experiments. Control (n=87), *kdm5[140]* (n=49), *Act5C>kdm5*-shRNA (n=79).
(B) Western blot of larval CNS material from control and *kdm5* knockdown *Act>kdm5*-shRNA showing expression of HA-tagged KDM5, γ tubulin, H3K4me3 and histone H3.
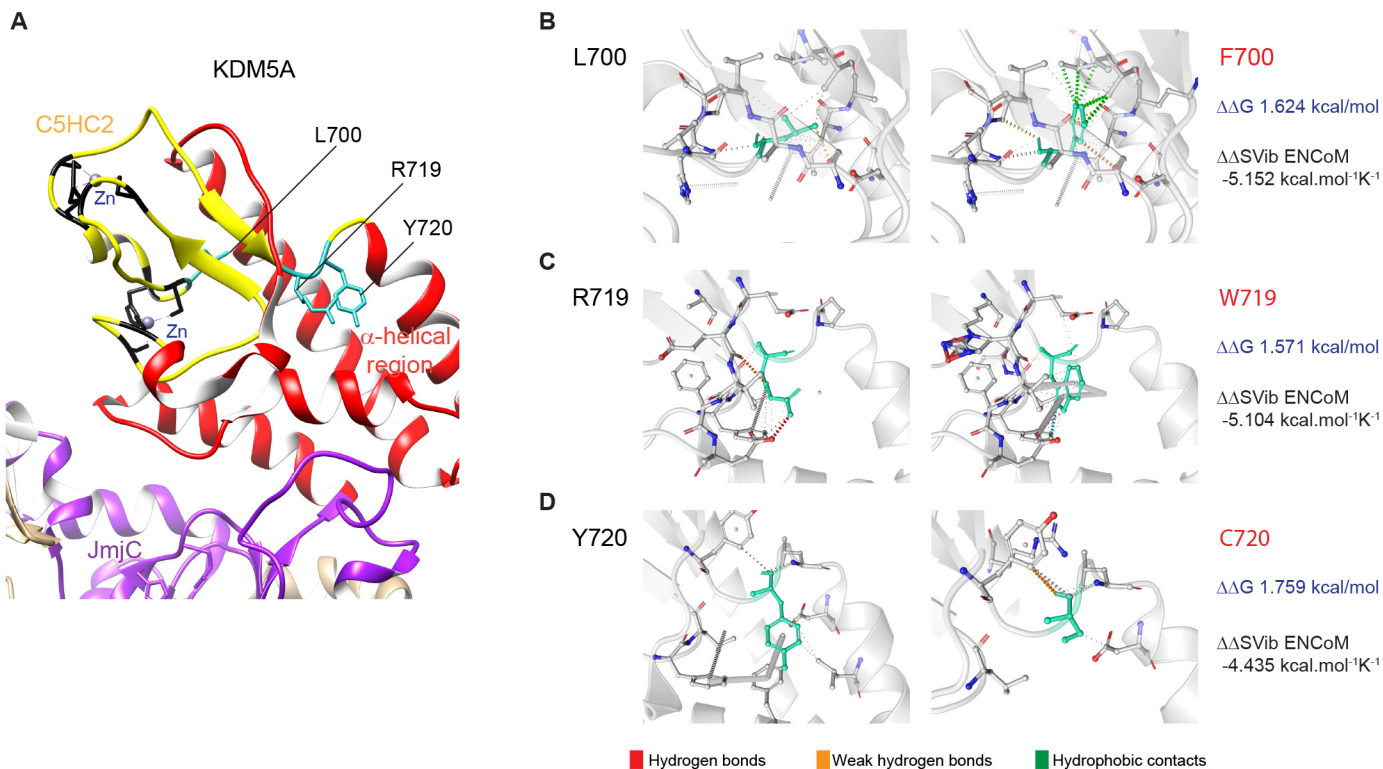
**Figure S2. ID mutations in the C5CH2 domain of KDM5 are predicted to change thermodynamic stabilization and molecule flexibility of the protein. Related to Figure 3.**

(A) Crystal structure of human KDM5A (PDB:5CEH) showing the amino acids altered by ID-associated mutations in the C5HC2 domain that were analyzed in this study.

(B-D) Predicted intramolecular interactions of the wild-type (left panel) L700 (B), R719 (C), Y720 (D) and mutated residues (right panel) F700 (B), W719 (C) and C720 (D) with the surrounding residue environment (corresponding amino acids in *Drosophila*: L854F, R873W, Y874C). The change in Gibbs free energy (DDG) calculated by DynaMut predicts stabilization of the structure for the three missense mutations (DDG$\geq$0). Calculations of the vibrational entropy energy ($\Delta\Delta$SVib) predict decrease of molecule flexibility for the three mutations ($\Delta\Delta$SVib<0).
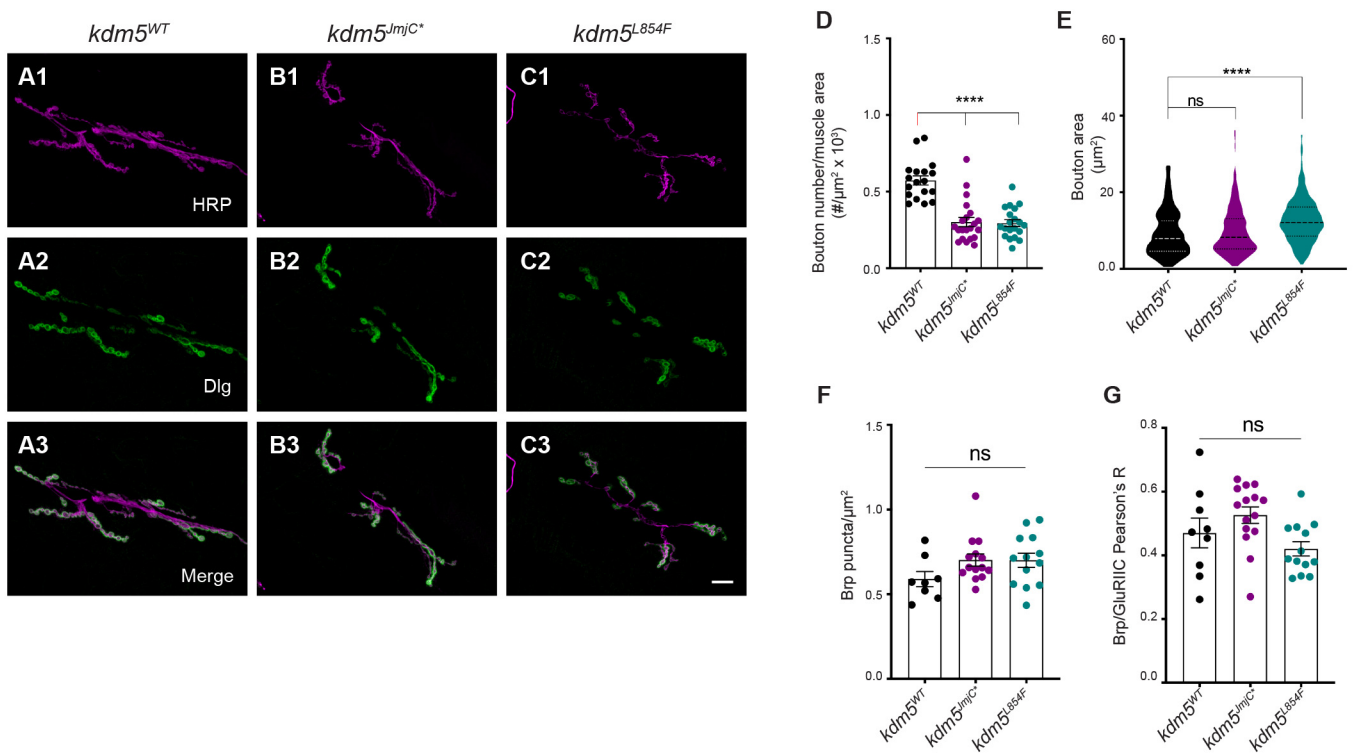
**Figure S3. *kdm5^JmjC^\* and *kdm5^L854F^* mutants display altered 6/7 NMJ morphology but do not change the number or localization of active zones. Related to Figure 5.**

(A1-C3) 6/7 NMJ morphology at abdominal segment 3 of third instar larvae labeled with HRP (magenta) and Dlg (green). Compared to *kdm5^WT^* (A1-3), *kdm5^JmjC^\** (B1-3) and *kdm5^L854F^* (C1-3) larvae display a reduction in the number of type Ib synaptic boutons. Scale bar, 20μm.

(D) Quantification of type Ib bouton number normalized to muscle surface area for *kdm5^WT^*, *kdm5^JmjC^\** and *kdm5^L854F^*. \*\*\*\**P*<0.0001. *kdm5^WT^* n=18, *kdm5^JmjC^\** n=21, *kdm5^L854F^* n=20.

(E) Quantification of type Ib bouton size. Violin plots show the frequency distribution of bouton surface area indicating the median and quartiles. \*\*\*\**P*<0.0001. *kdm5^WT^* n=306, *kdm5^JmjC^\** n=195, *kdm5^L854F^* n=160.

(F) Quantification of Brp density calculated as number of fluorescent puncta divided by total NMJ area. *kdm5^WT^* n=8, *kdm5^JmjC^\** n=14, *kdm5^L854F^* n=13.

(G) Quantification of Brp/GluRIIC apposition. *kdm5^WT^* n=9, *kdm5^JmjC^\** n=15, *kdm5^L854F^* n=13.

ns = not significant.